ALMA MATER STUDIORUM – UNIVERSITA' DI BOLOGNA

Scuola di Scienze

Laurea Magistrale in Fisica

Analysis of the scale effect in different computed tomography systems on the evaluation of bone tissue parameters

Tesi di laurea di:

ANTONELLA BIANCULLI

Relatore:

Prof.ssa MARIA PIA MORIGI

Correlatore:

Dott. FABIO BARUFFALDI

Anno Accademico 2015/2016

Di nuovo a Te, Nonna

questa volta forse di più…

…perché Ovunque tu sia,

io so Amare fin lì!

ABSTRACT

Tra le patologie ossee attualmente riconosciute, l'osteoporosi ricopre il ruolo di protagonista data le sua diffusione globale e la multifattorialità delle cause che ne provocano la comparsa. Essa è caratterizzata da una diminuzione quantitativa della massa ossea e da alterazioni qualitative della micro-architettura del tessuto osseo con conseguente aumento della fragilità di quest'ultimo e relativo rischio di frattura. In campo medico-scientifico l'imaging con raggi X, in particolare quello tomografico, da decenni offre un ottimo supporto per la caratterizzazione ossea; nello specifico la microtomografia, definita attualmente come "gold-standard" data la sua elevata risoluzione spaziale, fornisce preziose indicazioni sulla struttura trabecolare e corticale del tessuto. Tuttavia la micro-CT è applicabile solo in-vitro, per cui l'obiettivo di questo lavoro di tesi è quello di verificare se e in che modo una diversa metodica di imaging, quale la cone-beam CT (applicabile invece in-vivo), possa fornire analoghi risultati, pur essendo caratterizzata da risoluzioni spaziali più basse. L'elaborazione delle immagini tomografiche, finalizzata all'analisi dei più importanti parametri morfostrutturali del tessuto osseo, prevede la segmentazione delle stesse con la definizione di una soglia *ad hoc*.

I risultati ottenuti nel corso della tesi, svolta presso il *Laboratorio di Tecnologia Medica* dell'Istituto Ortopedico Rizzoli di Bologna, mostrano una buona correlazione tra le due metodiche quando si analizzano campioni definiti "ideali", poiché caratterizzati da piccole porzioni di tessuto osseo di un solo tipo (trabecolare o corticale), incluso in PMMA, e si utilizza una soglia fissa per la segmentazione delle immagini. Diversamente, in casi "reali" (vertebre umane

scansionate in aria) la stessa correlazione non è definita e in particolare

è da escludere l'utilizzo di una soglia fissa per la segmentazione delle

immagini.

CONTENTS

CHAPTER 3

- Analysis of structural and densitometric parameters of bone -

CHAPTER 4

- Experimental tests at the Laboratory of Medical Technology of "Rizzoli Orthopedic Institute" -

CHAPTER 5

- Analysis of Results -

CHAPTER 6

- Discussion of Results -

INTRODUCTION

The present thesis describes the results of the research work performed at the *Laboratory of Medical Technology* of Rizzoli Orthopedic Institute.

In recent decades, an issue that affects the medical-scientific studies of orthopedic character, through medical imaging, is undoubtedly inherent in the osteoporotic disease. Osteoporosis is a systemic disorder characterized by a quantitative decrease of bone mass and qualitative alterations of the micro-architecture of the bone tissue, which predispose to enhanced bone fragility resulting in an increased risk of fractures. The vertebrae and limb bones are the locations of the human body most affected and more susceptible to fracture. The fracture is realized when the load that the bone must support exceeds its capacity for resistance. Osteoporosis is defined as the most frequent metabolic disease of the skeleton and it occurs mainly in women in post-menopausal stage.

The main purpose of this thesis is to compare, through two different methods of tomographic imaging (micro-CT and cone beam CT with different spatial resolutions), the morpho-structural parameters characterizing the bone tissue, with a focus on cancellous bone. In particular, the aim is to investigate if and how the structural parameters concerning the bone tissue, calculated with the first method (taken as reference standard) can also be estimated from the other one.

The thesis is divided into six chapters. The first chapter concerns the description of bone human skeleton with its structural organization and its biology, while in the second chapter attention focuses on the most used bone imaging techniques and in particular on Computed Tomography. In the third chapter the main morphometric parameters, characterizing the bone micro-architecture, are described while in the fourth chapter the materials and the methods used for the purposes of the study are presented. The thesis concludes with the fifth chapter in which the obtained results are analyzed and plotted and with the sixth chapter in which the last considerations are done laying the foundations of what could be the future development of the conducted work.

CHAPTER 1
Bone Tissue characterization

1.1. Structure of bone tissue

The human skeleton consists of 206 bones. At birth, it is composed of 270 bones, but many of them fuse together as a child grows up. The main constituent of the skeleton is bone and its fundamentals functions are to provide support, to give our bodies' shape, to provide protection to other systems and organs of the body, to provide attachments for muscles, to create movement and to produce red blood cells.

The skeletal system includes also connective tissue that differs from bone because this latter has characteristics of rigidity and hardness. The human skeleton can be divided into the axial skeleton and the appendicular skeleton.

The axial skeleton is formed by about 80 bones: the vertebral column (32-34 bones), the rib cage (12 pairs of ribs and the sternum), the skull (22 bones) and other associated bones. It maintains the upright posture of humans. The appendicular skeleton, connected to the axial skeleton, is formed by 126 bones and in particular by the shoulder girdle, the pelvic girdle and the bones of the upper and lower limbs. Their functions are to allow to walk and to protect the major organs of digestion, excretion and reproduction.

Anatomical differences between human males and females are strongly marked in some soft tissue areas, but they tend to be limited in the skeleton. The human skeleton hasn't sexual different shapes as that of many other primate species, but delicate differences between genders in the morphology of the skull, dentition, long bones, and pelvis are exhibited across human populations. In general, female skeletal

elements appear to be smaller and less robust than corresponding male elements within a given population.
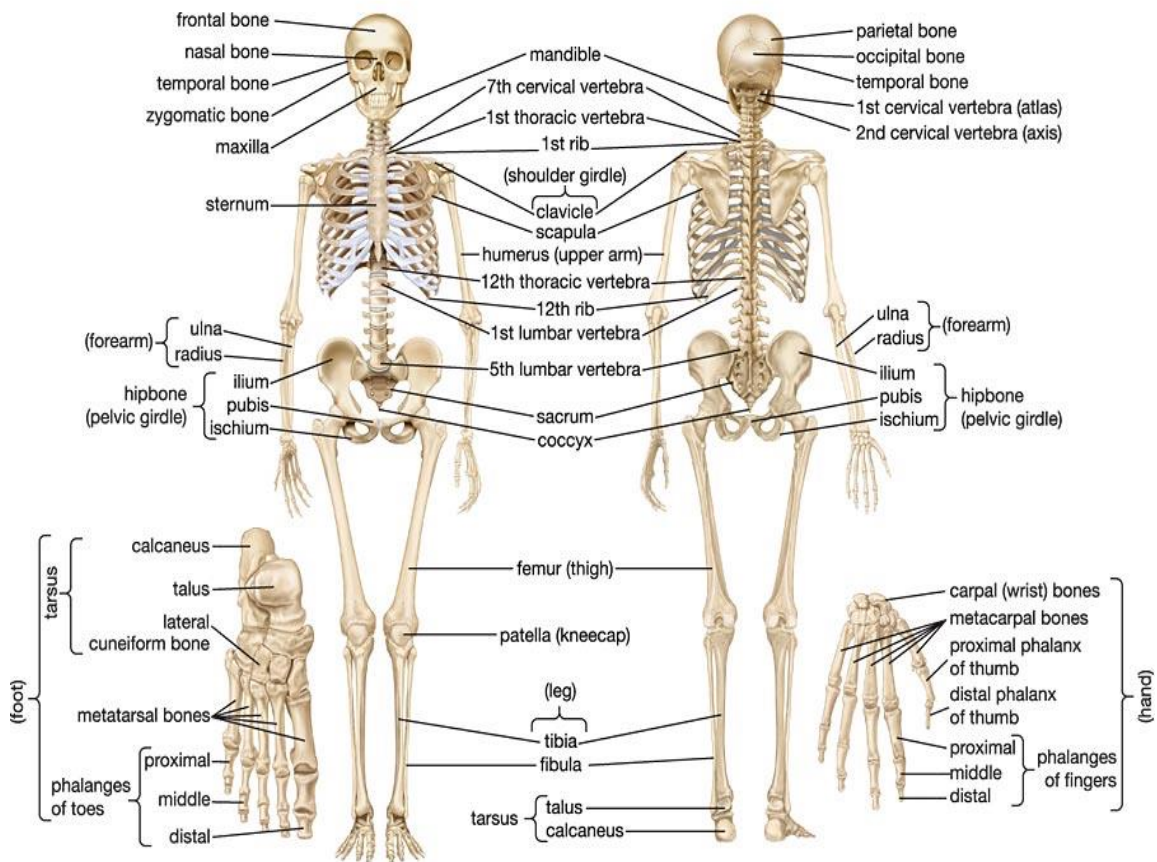
Fig. 1- A anterior and posterior view of the human skeletal system.

1.2. Biology of bone tissue

Bone is a mineralized connective tissue that is characterized by four types of cells: osteoblasts, bone lining cells, osteocytes, and osteoclasts (Buckwalter, Glimcher, Cooper, & Recker, 1996).

Osteoblasts are cuboidal cells that are placed along the bone surface comprising 4–6% of the total present bone cells and are mainly known for their bone forming function. These cells show morphological characteristics of protein synthesizing cells, including abundant rough endoplasmic reticulum and prominent Golgi apparatus (Florencio-Silva

et al., 2015). As polarized cells, the osteoblasts secrete, as different specific proteins, the osteoid toward the bone matrix. Osteoid is the organic portion, initially unmineralized, of the bone matrix that forms prior to the maturation of bone tissue.

The synthesis of bone matrix by osteoblasts comes in two main steps: deposition of organic matrix and its subsequent mineralization. In the first step, the osteoblasts secrete collagen proteins, mainly type I collagen, non-collagen proteins and proteoglycan including decorin and biglycan, which form the organic matrix. Thereafter, mineralization of bone matrix splits into two phases: the vesicular and the fibrillar phases (Anderson, 2003). The vesicular phase takes place when portions with a flexible diameter with a range from 30 to 200 nm, called matrix vesicles, are liberated from the apical membrane domain of the osteoblasts into the new formed bone matrix in which they bind to proteoglycans and other organic components. Given their negative charge, the sulphated proteoglycans immobilize calcium ions that are stored within the matrix vesicles (Yoshiko, Candeliere, Maeda, & Aubin, 2007). When osteoblasts secrete enzymes that deteriorate the proteoglycans, the calcium ions are released from the proteoglycans and cross the calcium channels displayed in the matrix vesicles membrane. Furthermore, phosphates are degraded by the ALP secreted by osteoblasts that release phosphate ions inside the matrix vesicles. Then, the phosphate and calcium ions contents the vesicles nucleate, forming the hydroxyapatite crystals (Florencio-Silva et al., 2015). The fibrillar phase takes place when the supersaturation of calcium and phosphate ions inside the matrix vesicles conducts to the rupture of these structures and the hydroxyapatite crystals spread to the surrounding matrix. Osteoblasts become mature and, at this moment, it can undergo apoptosis or become osteocytes or bone lining cells.

Osteoclasts are differentiated multinucleated cells, which originate from mononuclear cells of the hematopoietic stem cell lineage, under the influence of several factors that promote the activation of transcription factors and gene expression. They are responsible for the breakdown of bones. The breakdown of bone is very important in bone health because it allows for bone remodelling. The osteoclast disassembles and digests the composite of hydrated protein and mineral at a molecular level by secreting acid and a collagenase; this process is named bone resorption. In addition to its main function, the process also helps regulate the level of blood calcium. Osteoclasts are vital to the process of bone growth, the rebuilding of bone, and the bone's ability to repair itself.

Osteocytes, which comprise 90–95% of the total bone cells, are the most abundant and long-lived cells, with a half-life of about 25 years (Franz-Odendaal, Hall, & Witten, 2006). The cell body varies from 5 to 20 micrometers in diameter and contain 40-60 cell processes per cell, with a cell-to-cell distance between 20-30 micrometers. Different from osteoblasts and osteoclasts, which have been defined mainly for their core functions during bone formation and bone resorption, osteocytes were initially defined by their morphology and location. With the development of new technologies such as the identification of osteocyte-specific markers or new techniques for bone cell isolation, it has been recognized that these cells play numerous important functions in bone. When osteoblasts become trapped in the matrix that they secrete, they become osteocytes. Osteocytes are networked to each other via long cytoplasmic extensions that occupy tiny canals called canaliculi, which are used for exchange of nutrients and waste through gap junctions. They are able to molecular synthesis and modification, as transmission of signals over long distances, in a way similar to the

nervous system. Osteocytes contain glutamate transporters that produce nerve growth factors after bone fracture. When osteocytes are experimentally destroyed, the bones show a significant increase in bone resorption, decreased bone formation, trabecular bone loss, and loss of response to unloading (Noble, 2008). The osteocyte is an important regulator of bone mass and a key endocrine regulator of phosphate metabolism.

Bone-lining cells are inactive flat-shaped osteoblasts that cover the bone surfaces, where neither bone resorption nor bone formation occurs. Bone lining cells functions are not completely understood, but it has been shown that these cells allow the direct interaction between osteoclasts and bone matrix and participate in osteoclasts differentiation. They allow the osteoclasts access to mineralized tissue. Bone-lining cells occupy the majority of the adult bone surface and they are responsible for the immediate release of calcium in the bone if calcium in the blood is too low (Cowin & Telega, 2003).

1.3. Osteogenesis

There are two modes of bone formation, called also osteogenesis, and both involve the transformation of a pre-existing mesenchymal tissue into bone tissue. This direct conversion is called intramembranous ossification. This process occurs initially in the bones of the skull. In other cases, the mesenchymal cells differentiate into cartilage, and this cartilage is later replaced by bone. The process by which a cartilage intermediate is formed and replaced by bone cells is called endochondral ossification.

The Intramembranous ossification is the process responsible for the formation of the flat bones of the skull. During intramembranous ossification in the skull, neural crest-derived mesenchymal cells grow

rapidly and condense into compact nodules. Some of these develop into capillaries; others change their shape to become osteoblasts, committed bone precursor cells (Fig.2-A). The osteoblasts secrete a collagen-proteoglycan matrix that is able to attach calcium salts: the prebone (osteoid) matrix becomes calcified. In most cases, osteoblasts are separated from the region of calcification by a layer of the osteoid matrix they secrete. As calcification proceeds, bony spicules radiate out from the region where ossification began (Fig.2-B). Furthermore, the entire region of calcified spicules becomes surrounded by compact mesenchymal cells that characterize the periosteum (a membrane that surrounds the bone). The cells on the inner surface of the periosteum also become osteoblasts and deposit osteoid matrix parallel to that of the existing spicules. In this manner, many layers of bone are formed (Gilbert SF. Developmental Biology., 2000).
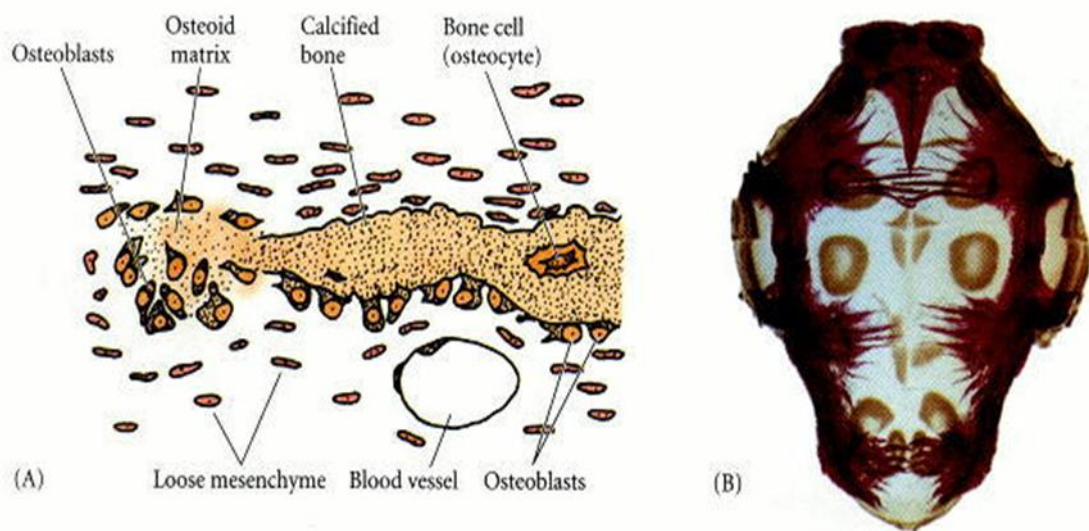
Fig.2 - Schematic diagram of intramembranous ossification. (A) Mesenchymal cells condense to produce osteoblasts, which deposit osteoid matrix. These osteoblasts become arrayed along the calcified region of the matrix. Osteoblasts that are trapped within the bone matrix become osteocytes. (B) An example of intramembranous ossification forming the turtle shell.

Endochondral ossification involves the formation of cartilage tissue from aggregated mesenchymal cells, and the subsequent replacement of cartilage tissue by bone (Horton W A., 1990). It is an essential process during the rudimentary formation of long bones, the growth of the length of long bones, and the natural restoring of bone fractures. The mechanism is very laborious with the implication of many factors that are beyond my thesis, so Fig. 3 explains a schematic diagram of endochondral ossification.
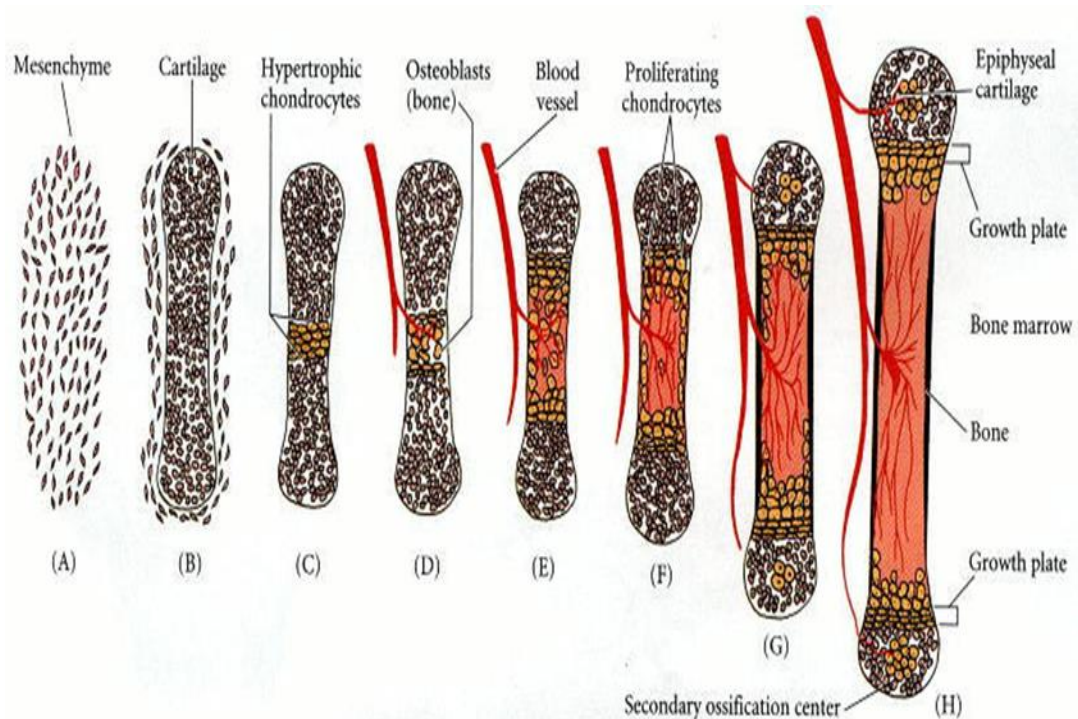
Fig. 3 - Schematic representation of endochondral ossification process. A, B) Mesenchymal cells condense and differentiate into chondrocytes to form the cartilaginous model of the bone. (C) Chondrocytes in the center of the shaft undergo hypertrophy and apoptosis while they change and mineralize their extracellular matrix. Their deaths allow blood vessels to enter. (D, E) Blood vessels bring in osteoblasts, which bind to the degenerating cartilaginous matrix and deposit bone matrix. (F-H) Bone formation and growth consist of ordered arrays of proliferating, hypertrophic, and mineralizing chondrocytes. Secondary ossification centres also form as blood vessels enter near the tips of the bone.

1.4. Bone structural organisation

To appreciate the mechanical properties of bone material, it is important to investigate the various levels of hierarchical structural organization of bone. These levels and structures are:

•   the macrostructure: cancellous and cortical bone;

•   the microstructure (from 10 to 500 μm): Haversian systems, osteons, single trabeculae;

•   the sub-microstructure (1–10 μm): lamellae;

•   the nanostructure (from a few hundred nanometers to 1 μm): fibrillar collagen and embedded mineral;

•   the sub-nanostructure (a few hundred nanometers): molecular structure of constituent elements, such as mineral, collagen, and non-collagenous organic proteins.

Bone is not a uniformly solid material. Human skeleton is composed of two types of osseous tissues whose difference consists in their structure and distribution and that are designed to perform different functions.

The hard outer layer of bones is constituted by cortical bone also called compact bone. The word cortical refers to the exterior (cortex) layer. The hard exterior layer gives bone its smooth, white, and solid appearance; it is much denser than cancellous bone, stronger and stiffer. Cortical bone provides about 80% of the weight of a human skeleton. At microscope cortical bone consists of multiple columns, each called an osteon. Each column is structured of layers of osteoblasts and osteocytes around a central canal called the Haversian canal. Around it, there are concentric rings (lamellae) of matrix. Volkmann's canals connect the osteons together. Between the rings of matrix, the bone cells (osteocytes) are placed in spaces called lacunae. Small channels (canaliculi) diffuse from the lacunae to the osteonic (Haversian) canal

to supply passageways through the hard matrix. The osteonic canals contain blood vessels that are parallel to the long axis of the bone. These blood vessels interconnect, through perforating canals, with vessels on the surface of the bone.
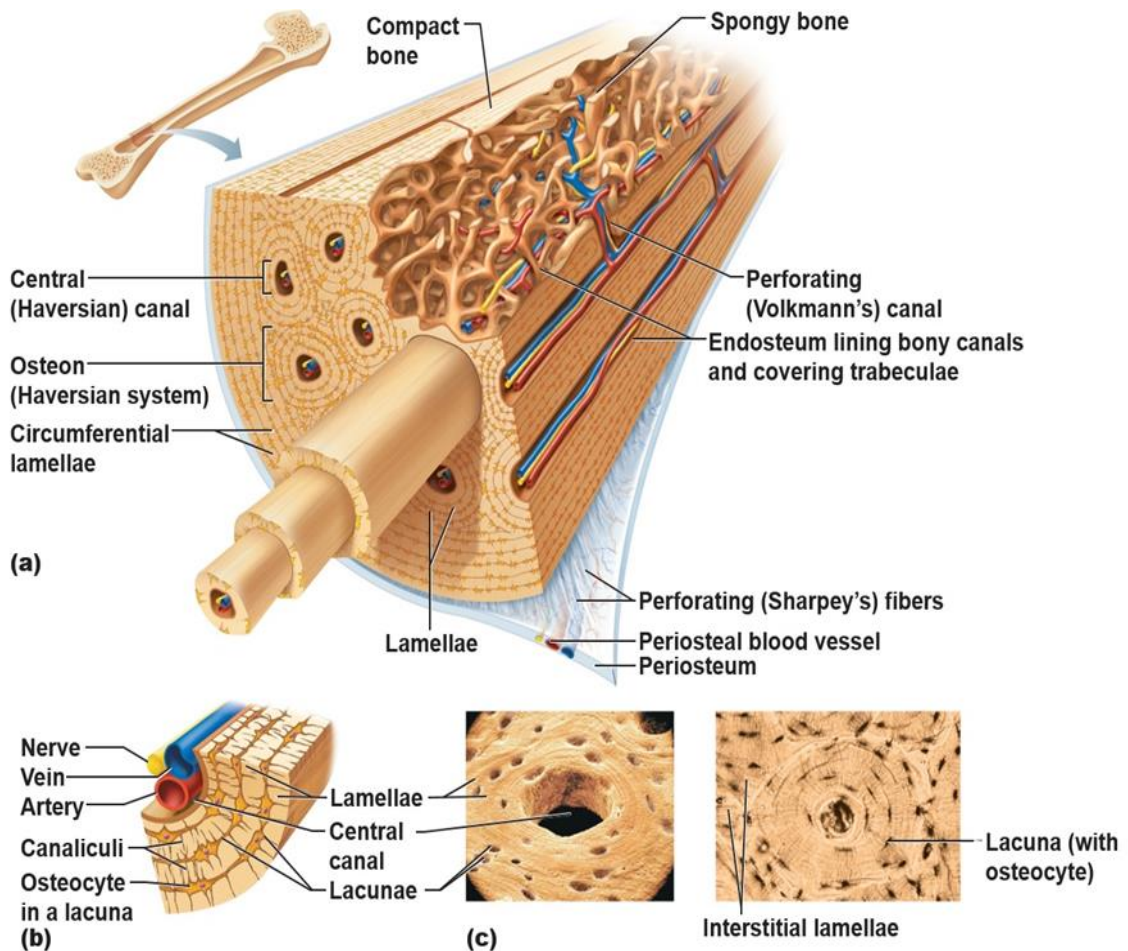
Fig. 4 – (a) Microscopic Anatomy of Bone. (b) Canaliculi connect lacunae to each other and the central canal. (c) Lacunae, small cavities that contain osteocytes

The major functions of cortical bone are to support the whole body weight, to protect organs, to provide levers for movement, to store and release calcium.

Cancellous bone is also called trabecular bone or spongy bone. Compared to cortical bone, it has a higher surface area but is less dense,

softer, weaker, and less stiff. It typically occurs at the ends of long bones, proximal to articulations and within the interior of vertebrae. Microscopically, cancellous bone consists of plates (trabeculae) and other irregular cavities that contain bone marrow. The trabeculae of spongy bone succeed the lines of stress and can realign if the direction of stress changes. It may appear that the trabeculae are arranged in an irregular manner, but they are organized to provide maximum strength. Thanks to its greater surface area, cancellous bone is ideal for metabolic activity, e.g. exchange of calcium ions.

1.4.1. Types of bone

There are five types of bones in the human body classified by shape: long, short, flat, irregular, and sesamoid. *Long bones* are composed by a shaft, the diaphysis, which is much longer than its width, and by an epiphysis, a rounded head at the end of the shaft. They are made up mostly of compact bone, with lesser amounts of marrow, located within the medullary cavity, and cancellous bone. Most bones of the limbs, including fingers and toes, are long bones. *Short bones* are irregularly cube-shaped, and have only a thin layer of compact bone surrounding a spongy interior. An example of short bones are the wrist and ankle. *Flat bones* are thin, generally curved, with two parallel layers of compact bones and, in the middle, a layer of spongy bone. Most of the bones of the skull are flat bones, as is the sternum. *Sesamoid bones* are bones implanted in tendons. Examples of sesamoid bones are the patella and the pisiform. *Irregular bones* do not fit into the categories mentioned until now. They consist of thin layers of external compact bone with a spongy bone within. Their shapes are irregular and complex. The bones of the spine, pelvis, and some bones of the skull are irregular bones.

1.5. Bone turnover and development

1.5.1. Bone resorption

Bone resorption is a process consisting in the breakdown of bone by specialized cells known as osteoclasts. It occurs on a continual level inside the body, with the destroyed bone replaced by new bone growth. Osteoclasts work by attaching themselves to individual bone cells and secreting compounds to break the cells, with subsequent release of their mineral contents. The minerals enter the bloodstream, where they are processed for recycling of new bone or eliminated with other bodily wastes. Osteoclasts break bone consequently to inflammation, disease and injury, removing damaged bone to allow it to be replaced with new bone. In cases where bone resorption becomes accelerated, bone is broken down faster than it can be renewed. The bone becomes more porous and fragile, facilitating the risk of fractures.

1.5.2. Bone remodeling

Bone remodeling, called also bone metabolism, is an important process that occurs throughout a person's lifetime; ossification and resorption work together to reshape the skeleton during growth, to maintain calcium levels in the body and to repair micro-fractures caused by quotidian stress. During the bone remodeling process, bone-making cells called osteoblasts deposit new bone and osteoclasts absorb the old bone. The remodelling has both positive and negative effects on bone tissue quality. It allows removing micro-damage, replacing dead and hypermineralized bone and adapting the microarchitecture to local stress. However, remodelling may also perforate or remove trabeculae, increase cortical bone porosity, decrease cortical width and possibly reduce bone strength.

1.6. Bone disease

Bone disease is a condition that injures the skeleton, makes bones weak and prone to fractures. Despite strong bones are structured in childhood, people, in every part of their life, can improve their bone health. The most common bone disease is osteoporosis, which is characterized by low bone mass and deterioration of bone structure. Low bone mass is when bones lose minerals, like calcium, and as consequence, bones become weak and fracture easily. Calcium is an essential mineral needed by the body to build strong bones and to keep them strong throughout the life. Calcium is also needed for other purposes, such as muscle contraction. Almost all calcium (99 percent) is stored in the bones. The remaining one percent circulates in the body. 'Osteoporosis' literally means 'porous bones' and is often referred to as the 'fragile bone disease' in an increased risk of fractures of the hip, spine, and wrist with consequences for the bone mechanics. Osteoporosis is often called a "silent" disease because it has no discernible symptoms until there is a bone fracture.

Many factors lead to fractures: age, heredity, body weight, diseases, lifestyle, frailty, and amount of trauma all play important roles. Osteoporosis can be prevented, as well as diagnosed and treated. Fractures to weak bones typically occur from falling or other common accidents.
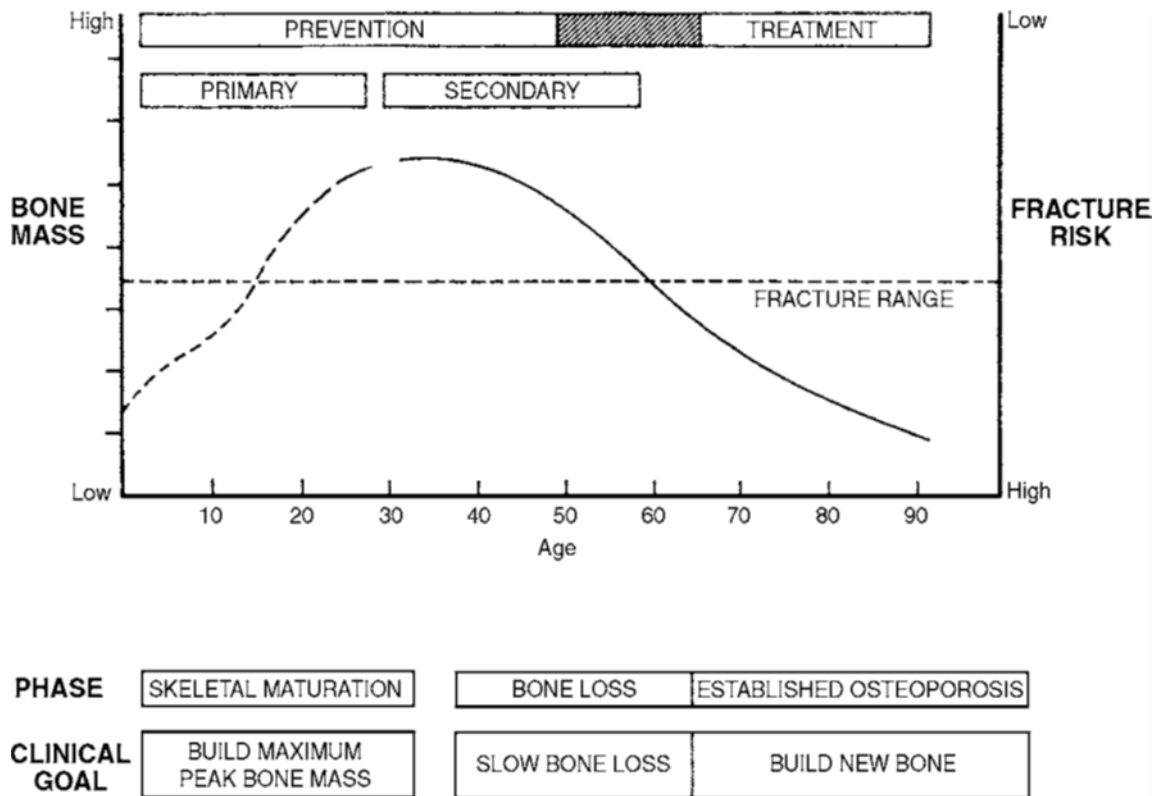
Fig. 5 - Diagram illustrating the course of bone gain and loss throughout life and fracture risk. Horizontal dotted line represents the level below which structural failures or fractures are likely to occur. This level is reached earlier in women than in men because of the differences in the magnitude of the age-related bone loss. In both sexes, level is reached earlier in those who accumulate less bone (peak bone mass) during growth (Clifford J. Rosen, Roger Bouillon, Juliet E. Compston, 2013).

The incidence of osteoporotic fractures is very high: in the USA, about 45% of postmenopausal women have low bone density. The lifetime risk of a fracture of the hip, spine or forearm is 40% in white women and 13% in white men. African-Americans have fewer fractures than people of other races. Worldwide the rates of osteoporosis are variable, but in every country, age is one of the most important risk factors. As more people live longer lives, the number of those with osteoporosis will also increase (Melton, 1992).
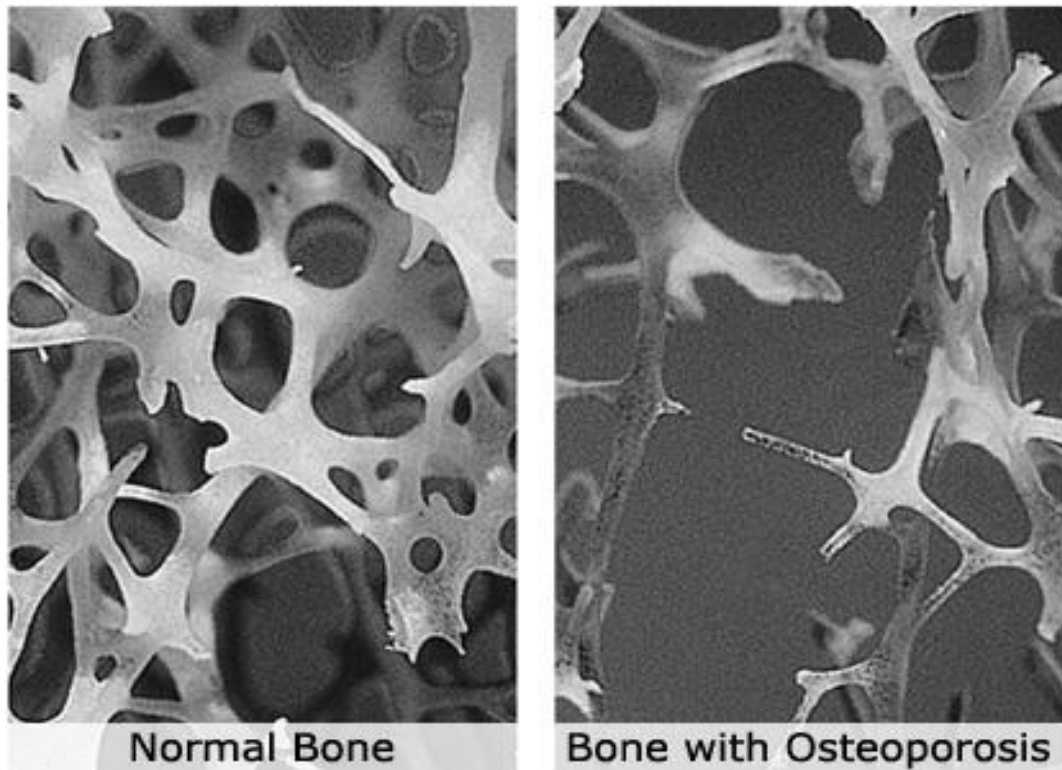
Fig. 6 - Trabecular bone structure in the lower spine of a young adult compared to an osteoporotic elderly adult.

Other bone diseases include Paget's disease and osteogenesis imperfecta. Paget's disease affects older men and women, and causes skeletal deformities and fractures. Osteogenesis imperfecta is an inherited disorder that causes brittle bones and frequent fractures in children.

CHAPTER 2

Imaging Techniques of Bone and its structures

Medical imaging is the technique and process that allows to have visual representations of the interior of a body for clinical analysis and medical intervention, for example a representation of the function of some organs or tissue. Currently, this ability to get information about the human body has many clinical applications. In the last decades, different sorts of medical imaging have been developed, each with its own advantages and disadvantages. The most used is imaging with X-ray based methods, but not less relief, especially in recent years, has been attributed to other types of medical imaging such as magnetic resonance imaging (MRI) and ultrasound imaging. The success of these techniques is due to the fact that they operate without ionizing radiation. MRI uses strong magnetic fields, which do not produce known irreversible biological effects in humans. Diagnostic ultrasound systems use high-frequency sound waves to create images of soft tissue and internal body organs.

2.1. X-ray radiation

X-radiation is a form of electromagnetic radiation with a wavelength in the range from UV rays (longer) and Gamma rays (shorter). The term "X-radiation" was first coined by its discover, Wilhelm Röntgen, who named it in this way to connote an unknown type of radiation.

Due to their penetrating ability, X-rays are largely used to image the inside of objects, e.g. in medical radiography.

X-ray photons transport energy sufficient to ionize atoms and disintegrate molecular bonds: this makes them a type of ionizing radiation. A very high radiation dose delivered in a short time generates radiation sickness, while lower doses can give an increased risk of cancer induced by radiation. In medical imaging this risk is generally greatly outweighed by the benefits of the examination. The ionizing capability of X-rays can be utilized in cancer treatment to kill malignant cells using radiation therapy. X-rays can traverse relatively thick objects without being much absorbed or scattered. For this reason. X-rays are widely used to image the inside of opaque objects and the "penetration depth" varies by several orders of magnitude over the X-ray spectrum. X-rays interact with matter in different ways: photoabsorption, Compton scattering, Rayleigh scattering, pair production. The strength of these interactions depends on the energy of the X-rays and the composition of the material. Photoabsorption or photoelectric absorption is the dominant interaction mechanism in the soft X-ray regime and for the lower hard X-ray energies. At higher energies, Compton scattering dominates (Jerrold T. Bushberg, J. Anthony Seibert, Edwin M. Leidholdt Jr., 2002).

The scheme of an X-ray tube is represented in Fig. 7. A high voltage is needed to produce the required kinetic energy of the electrons emitted from the cathode. When these electrons bombard the heavy metal atoms of the anodic target, they interact with these atoms and transfer their kinetic energy to the target. In particular, the electrons interact with the outer-shell electrons of the target atoms elevating them to a higher energy level (excited). At this point, the outer-shell electrons immediately drop back to their normal energy state emitting infrared

radiation. The constant excitation and re-stabilization of outer-shell electrons causes heat inside the anodes of X-ray tubes. Generally, more than 99% of the kinetic energy of the accelerated electrons is converted to thermal energy, instead less than 1% is available for the production of X-radiation (Dendy, Heaton, & Cameron, 2001).
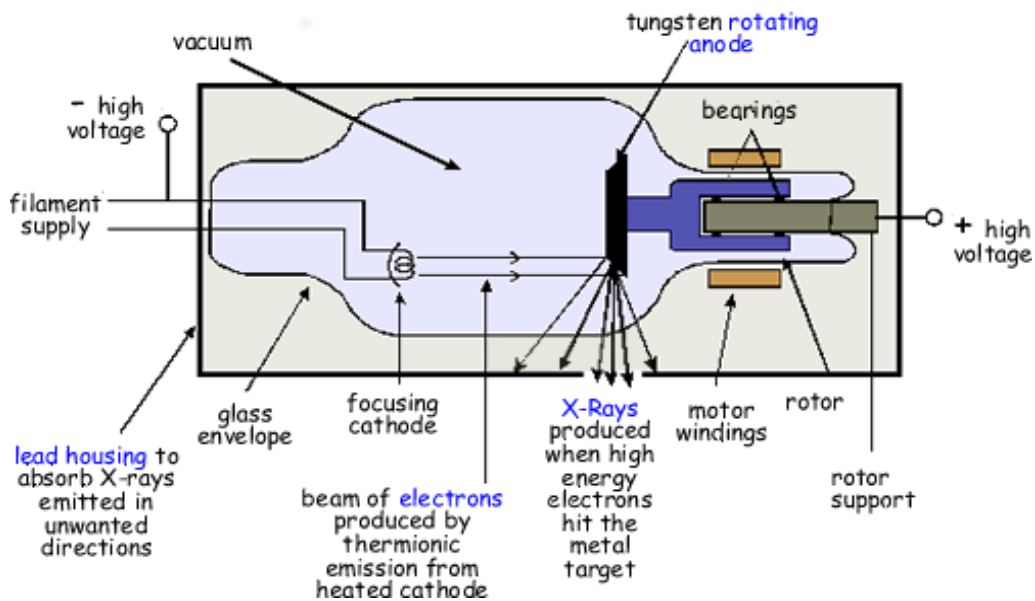
Fig. 7 – Essential features of a simple, stationary anode X-ray tube. For simplicity, only X-ray photons passing through the window are shown. In practice, they are emitted in all directions.

A typical X-ray spectrum is shown in Fig. 8 in which the two curves represent two different accelerating voltages. The X-ray spectrum can be divided in two parts: (a) a continuous background, and (b) a series of sharp peaks.
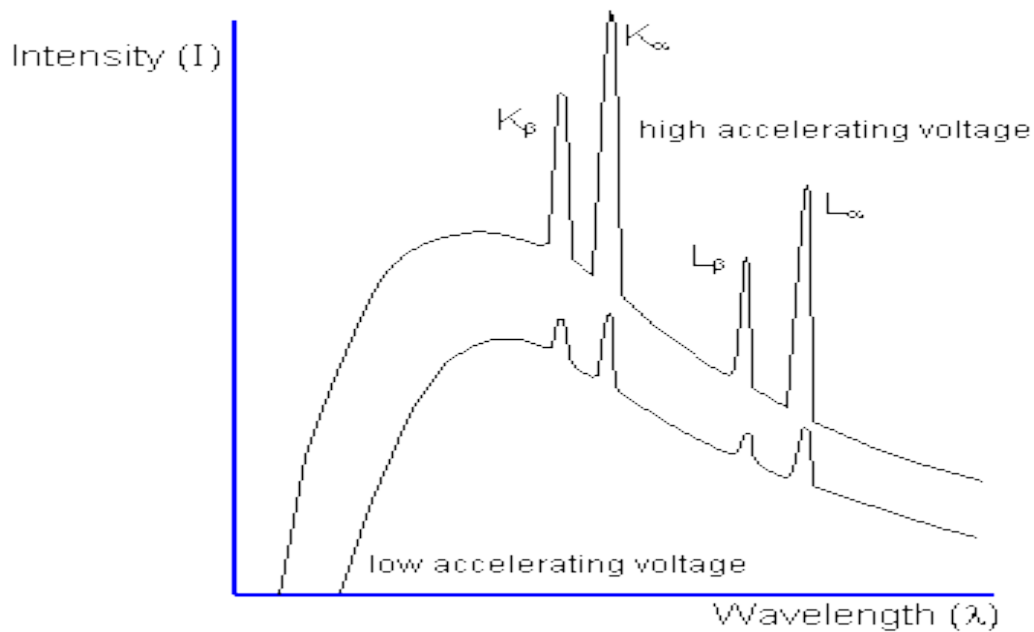
Fig. 8 Typical X-Ray spectrum with different voltages.

The electromagnetic attraction of the nuclei of the target material determines the electron slowdown and the consequent production of the so-called bremsstrahlung radiation. An X-ray photon with the minimum wavelength and therefore the maximum energy and frequency is produced when an electron is stopped by just one nucleus. The rest of the continuous curve in Fig. 8 is due to electrons that lose only part of their energy during collisions with many nuclei

$$\text{Minimum X ray wavelength } (\lambda) = hc/eV$$

where V is the accelerating voltage and c the velocity of light.

The peaks on the spectrum are characteristic of the particular target material. The bombarding electrons are able to ionize the target atoms by removing electrons from the inner shells. When this happens an electron from an outer energy level fills the vacancy emitting a photon of a definite wavelength, thus giving a sharp peak on the spectrum (Keith Gibbs, 2006).

21

The efficiency of X-ray production is independent of the tube current, but it increases with increasing electron energy. At 60 keV, only 0.5% of the electron kinetic energy is converted to X-rays; at 120 MeV, it is 70% (Fig.9) (Poludniowski, Landry, DeBlois, Evans, & Verhaegen, 2009).
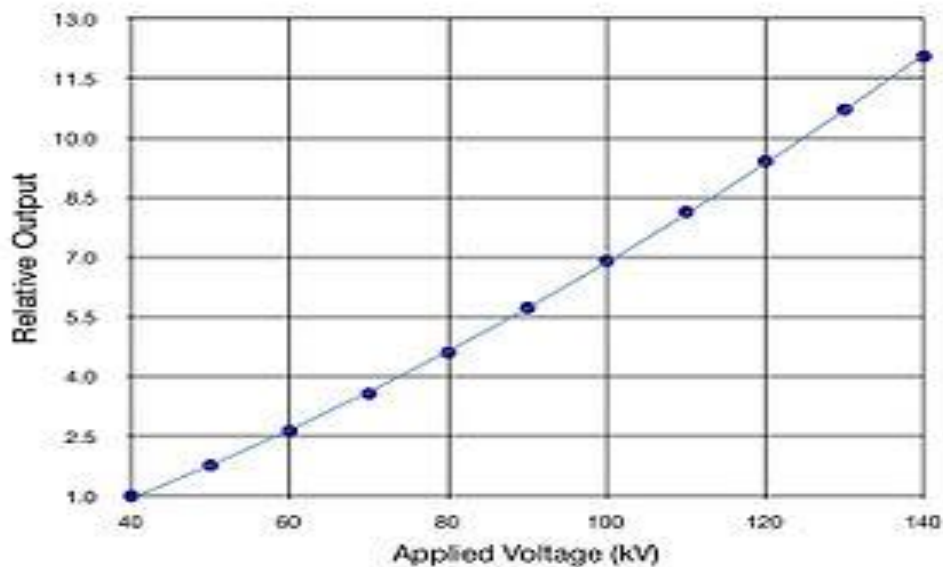

Fig.9 - Dependence of the output of an X-ray tube on applied voltage.

As already previously said, when X-rays are directed on an object, some photons interact with the particles of the matter and their energy can be absorbed or scattered. This absorption and scattering is called *attenuation.* Other photons proceed through the object without interacting with any of the material's particles. The number of photons transmitted depends on the thickness, density and atomic number of the material. If the photons have the same energy, they travel however at different distances within a material relying on the probability of their encounter with one or more of the particles of the matter and the modality of the interaction. Greater the distance traveled, greater the probability of collision with the particles; the number of photons

22

reaching a specific point within the matter decreases exponentially with distance traveled.
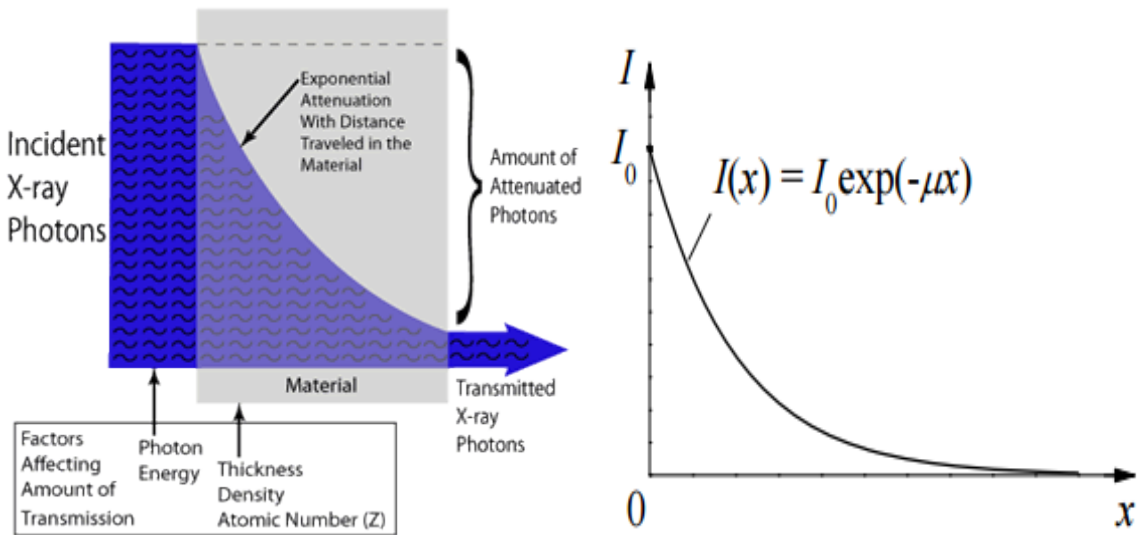
Fig. 10 - Dependence of X-ray radiation intensity on absorber thickness in case of a monochromatic X-ray beam (NDT Resource Center)

The formula that describes the curve shown in Fig. 10 is:

$$I = I_0 e^{-\mu x}$$

where:

- μ is the linear attenuation coefficient
- I is the intensity of photons transmitted across some distance x
- I_0 is the initial intensity of photons
- x is the distance traveled

The linear attenuation coefficient (μ) depends on the atomic number of the material, the density of the medium and the energy of the beam.

2.2. Computed Tomography

Among many medical imaging techniques, my thesis focuses on Computed Tomography (CT) that is a diagnostic imaging modality used to produce detailed images of internal organs, bones, soft tissue and blood vessels. In particular, Computer Axial Tomography (CAT) generates an image (CAT scan) of the tissue density in a "slice" as thin as 1 to 10 mm in thickness through the patient's body. The cross-sectional images generated during a CT scan can be reformatted in multiple planes, three-dimensional images can even generate and after they can be viewed on a computer monitor, or transferred to electronic media. Since its introduction in 1972 by Hounsfield, the use of CT has grown rapidly.

An X-ray source that rotates around the object generates X-ray slice data; X-ray sensors are positioned on the opposite side of the circle from the X-ray source. The earliest sensors were scintillation detectors, with photomultiplier tubes excited by (typically) cesium iodide crystals. Cesium iodide was replaced during the 1980s by ion chambers containing high-pressure Xenon gas. The first clinical CT images were produced at the Atkinson Morley Hospital in London in 1972. The very first patient examination using CT, offered credible proof of the effectiveness of the method by detecting a cystic frontal lobe tumor. CT was immediately and enthusiastically introduced in the medical field by the medical community and has often been referred as the most important invention in diagnostic radiology since the discovery of X-rays. In 1979, Godfrey Hounsfield and Allan Cormack, an engineer and a physicist, were awarded the Nobel Prize for medicine in recognition of their outstanding achievements. The EMI scanner (1973) was designed for brain scanning, and its applications were limited to the

head (Fig. 11). The pencil beam employed in the first generation scanner resulted in poor geometrical utilization of the X-ray beam and it required long scanning times. In the second-generation scanner, the X-ray beam was collimated to a 10-degree fan, which circumscribed an array of 8 to 30 radiation detectors, rather than the previous pencil beam with only a single detector. Despite the second-generation scanner also used the translate-rotate mechanical motion, which created many difficulties, the fan beam, crossing the patient, permitted to obtain multiple angles with a single translation (Fig.12).
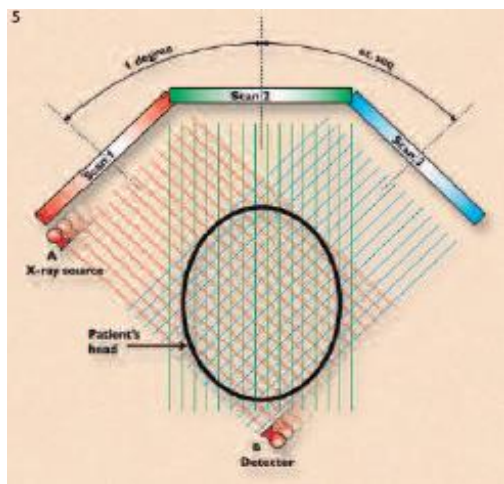
Fig. 11 - Illustration of the scanning sequence in a first-generation CT scanner
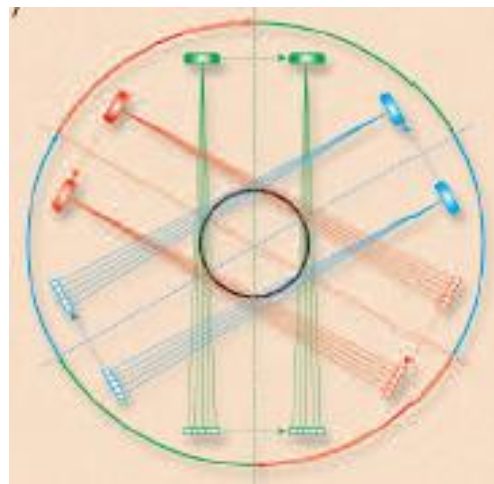
Fig.12 - Second-generation CT scanner

There are a limited number of beams (approximately 8 to 30) in a narrow fan configuration with the same translate-rotate motion used in first-generation machines. Each linear scan produces several projections at differing angles, one view for each X-ray beam. The fastest second-generation CT units could achieve a scanning time of 18 seconds per slice. The image quality was substantially improved. However, the second-generation units had definite speed limitations due to the inertia of the heavy X-ray tube and gantry during the complicated translate rotate motion. To improve speed, third- and

fourth-generation systems were built using rotation only. In the third-generation system, the X-ray tube and detector array are installed opposite one another and pivot around the patient in a single rotational movement during which the views are acquired (Fig. 13). In fourth-generation systems (Fig.14), the detector array is a stationary circle, and only the X-ray tube rotates through a circle within the array. As many as 1,200 to 2,400 detectors may be used, compared with 500 to 700 in third-generation units.
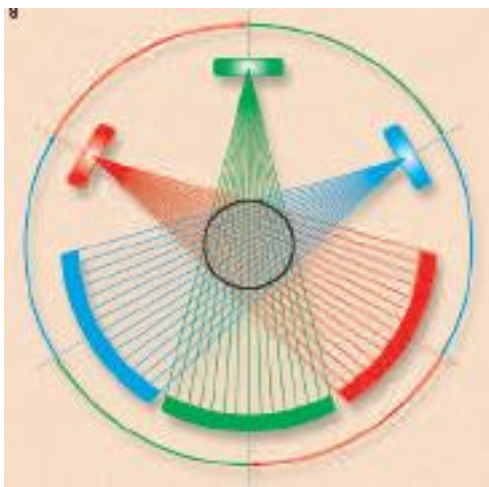
Fig.13 - Third-generation CT scanner   *Fig.14- Fourth-generation CT scanner*
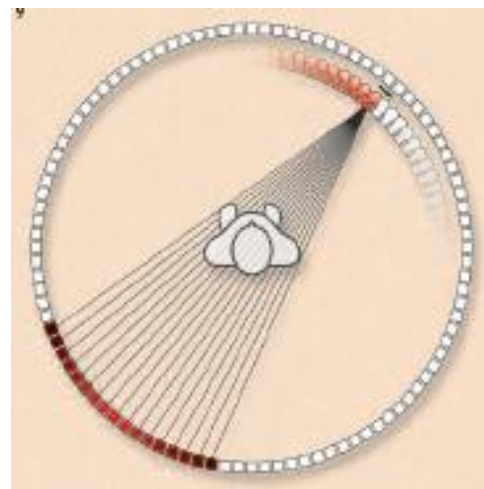
Both third- and fourth-generation scanners could obtain individual slices in 2 to 4 seconds. A variation on the fourth-generation design was the "ultrafast" CT scanner (Goldman, 2007).

After the fourth generation, there were no large variations in CT technology (other than incremental improvements) until 1987. CT examination times were dominated by inter-scan delays with results that were poor temporal resolution and long procedure times. Eliminating inter-scan delays required continuous rotation, a capability made possible by the low-voltage slip ring. A slip ring passes electrical power to the rotating components (e.g., X-ray tube and detectors) without fixed connections. An alternative strategy is to continuously rotate and

continuously acquire data as the table (patient) is smoothly moved though the gantry; the resulting trajectory of the tube and detectors relative to the patient traces out a helical or spiral path (Fig. 15). This powerful concept led to the construction of Helical CT (or Spiral CT) (Goldman, 2007).

However, the basic principles are similar for all techniques: all reconstructed cross-section images are based on the attenuation coefficients of the object that is examined.
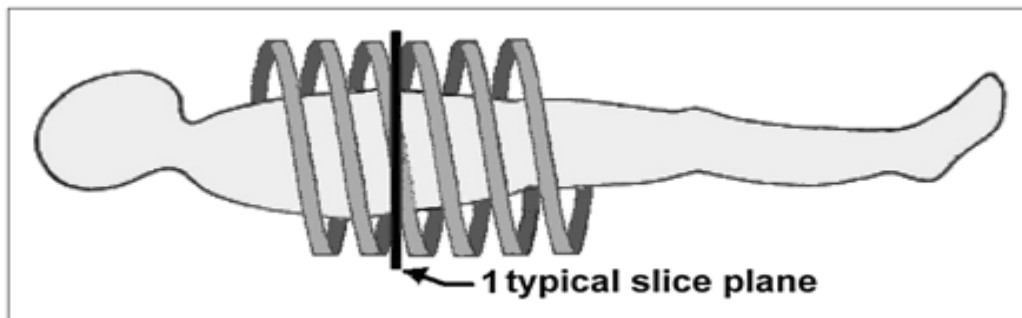
Fig. 15 - Helical CT. Improved body CT was made possible with advent of helical CT (or spiral CT). Patient table is moved smoothly through gantry as rotation and data collection continue. Resulting data form spiral (or helical) path relative to patient; slices at arbitrary locations may be reconstructed from these data.

Today, most modern hospitals currently use spiral CT scanners and beam types can be parallel beams, fan-beams, and cone-beams.

2.2.1 CT Reconstruction Algorithms

When talking about reconstruction algorithms, reference is made to four main methods aimed at computing the slice image given the set of its views. The first method is hardly workable, but provides a better

understanding of the problem. It is based on solving many **simultaneous linear equations**. One equation can be written for each measurement. That is, a particular sample in a particular profile is the sum of a particular group of pixels in the image. To calculate unknown variables (i.e., the image pixel values), there must be independent equations, and therefore N^2 measurements, if N×N is the size of the image.

The second method of CT reconstruction uses **iterative** techniques to calculate the final image in a few steps. There are several variations of this method: the Algebraic Reconstruction Technique (ART), the Simultaneous Iterative Reconstruction Technique (SIRT), and the Iterative Least Squares Technique (ILST). The difference between these methods is given by consequentiality of the corrections: ray-by-ray, pixel-by-pixel, or simultaneously correcting the entire data set, respectively. Iterative techniques are generally slow, but they are useful when better algorithms are not available.

The third method is called **filtered backprojection**. It is the most common used algorithm for computed tomography systems. It is a modification of an older technique, called **backprojection** or **simple backprojection.** Filtered backprojection is a technique to correct the blurring found in simple backprojection. Each of the one-dimensional views is convolved with a one-dimensional filter kernel to compose a set of *filtered views*. These filtered views are then backprojected to provide the reconstructed image. In fact, the image produced by filtered backprojection is *identical* to the "correct" image when there are an *infinite* number of views and an *infinite* number of points per view.

The fourth method is called Fourier reconstruction. In the spatial domain,

filtered view 1

filtered view 2

filtered view 3

a. Using 3 views

b. Using many views
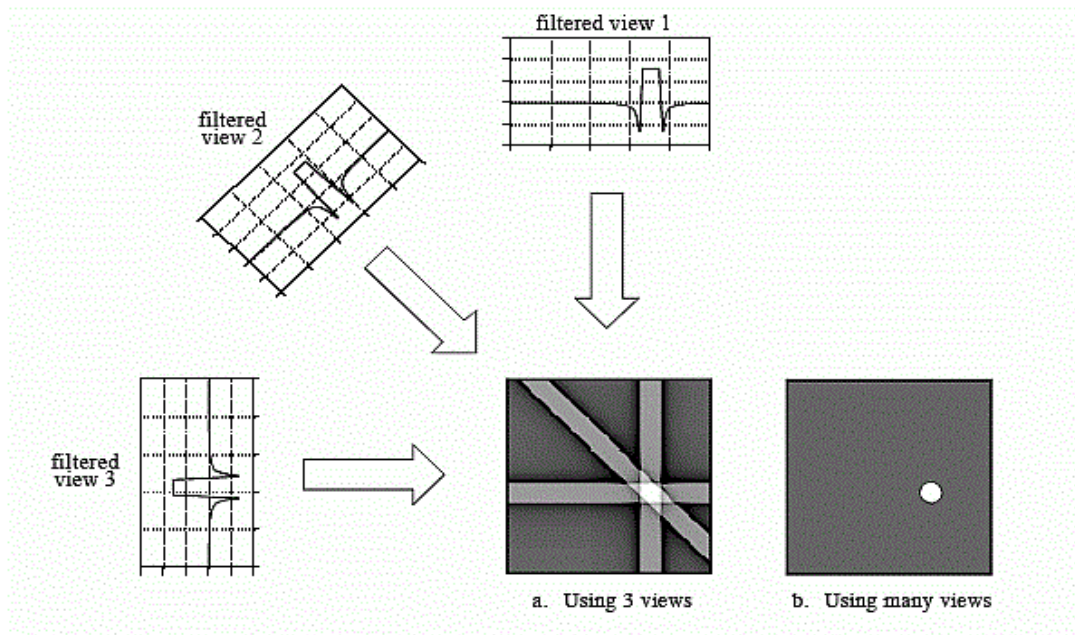
Fig. 16 – Filtered backprojection.

CT reconstruction involves the association between a two-dimensional image and its set of one-dimensional views. The frequency domain analysis of this problem is a milestone in CT technology called the Fourier slice theorem. It describes the relationship between an image and its views in the frequency domain. In the spatial domain, each view is found by integrating the image along rays at a particular angle. In the frequency domain, the spectrum of each view is "one-dimensional" slice of the two-dimensional image spectrum (Smith, 1999).
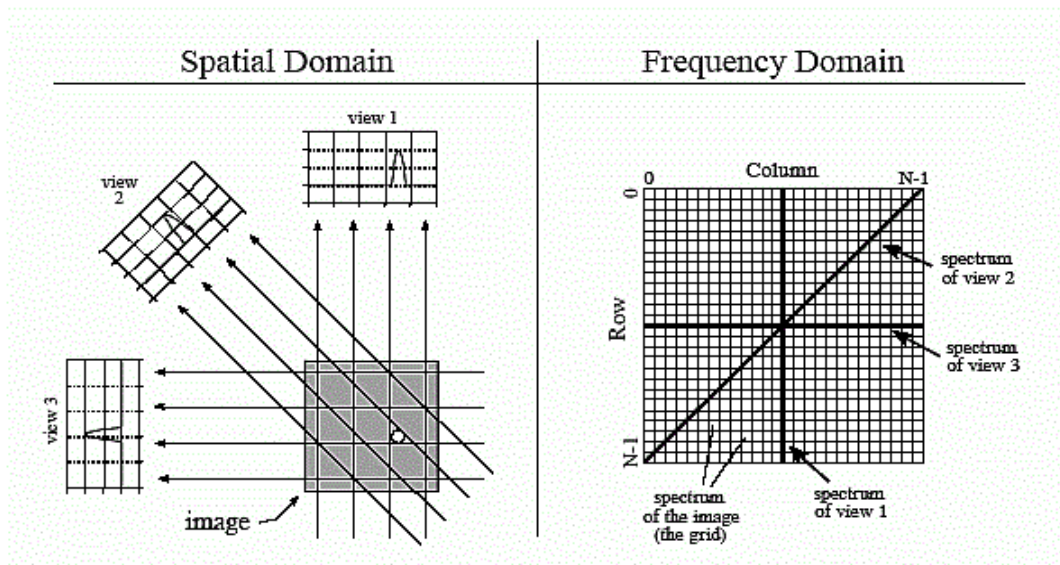
Fig.17- The Fourier Slice Theorem.

2.2.2. CT Imaging Techniques

X-ray projection images are still useful to analyse changes in cancellous bone architecture. Non-destructive imaging techniques, such as X-ray tomography (CT) and magnetic resonance imaging (MRI), allow investigating the three-dimensional structure of bone. Standard equipment, however, has limiting factors for the visualization of the microscopic features of bone, especially for in-vivo imaging. These limitations are primarily given by spatial resolution and, in the case of CT, also by patient's exposure to X-rays. The spatial resolution is one of the most important features for the quantification of the bone microarchitecture. In general, for the techniques actually available, spatial resolution and sample size are linked together (Perilli, 2006). Special systems were developed, such as micro-CT or micro-MRI, which allow the examination of small structures and details in three dimensions, and are suitable for the imaging of the trabecular structure. Different CT scanner configurations were developed in the last decades, by which either the source-detector system or the object are moving,

the number of detectors are augmented, with the principal aim to reduce scan-time (Kak, Author, Slaney, Wang, & Reviewer, 2002). Below, a little summary of typical and most used 3D-imaging procedures is reported.

2.2.2.1. Cone beam computed tomography

Cone-beam computed tomography (CBCT) is a medical imaging technique characterized by a CT set-up with cone-beam geometry and a two-dimensional detector. CBCT has become increasingly important for treatment planning and diagnosis in implant dentistry and interventional radiology (IR). It provides sub-millimetre resolution in images of high diagnostic quality, with brief scanning times (10–70 seconds) and radiation dosages reportedly up to 15 times lower than those of conventional CT scans (Scarfe, Farman, & Sukovic, 2006). Cone-beam technology was first introduced in the European market in 1996 by QR s.r.l. (Verona, Italy).

Fig.18- An example of CBCT machine

2.2.2.2. Micro-CT

Micro–computed tomography (micro-CT or μCT) has applications both in medical imaging and in the industrial field. The first X-ray microtomography system was idealised and built by Jim Elliott in the early 1980s. The first published X-ray microtomographic images were reconstructed slices of a small tropical snail, with pixel size about 50 micrometers (Elliott & Dover, 1982). The prefix *micro-* (symbol μ) is used to indicate that the pixel size of the cross-sections is in the micrometer range. In general, the system consists of a microfocus tube, which generates a cone-beam of X-rays, a rotating specimen holder, on which the object is positioned and a detector system that acquires the images. Differently from medical CT, in the micro-CT, the source-detector system is fixed, while the images are taken with the specimen rotating on a turntable. Typically, it is used for small animals (*in vivo* scanners), biomedical samples, foods, microfossils and other studies for which minute details are desired. Today, systems with spatial resolutions in the order of few μm or even better are available (http://www.skyscan.be (2006)). It is important to say that the spatial resolution during a scan with a cone-beam geometry is strictly related to the size of the object in examination.

Fig.19 – An example of Micro-CT device on the market.

2.2.2.3. *Quantitative Computed Tomography*

Quantitative computed tomography (QCT) is a medical technique that measures bone mineral density (BMD) using a standard X-ray Computed Tomography (CT) scanner with a standard calibration capable to convert Hounsfield Units (HU) of the CT image to BMD values. Quantitative CT scans are primarily used to evaluate bone mineral density at the lumbar spine and hip. QCT exams are typically used in the diagnosis and monitoring of osteoporosis. Today, modern 3D QCT uses the ability of CT scanners to rapidly acquire multiple slices to construct three-dimensional images of the human body. The use of 3D imaging is fundamental to reduce image acquisition time, to improve reproducibility and to enable QCT bone density analysis of the hip (Adams, 2009). An important role, furthermore, is played by **peripheral quantitative computed tomography**, that, as the name implies, is a type of quantitative computed tomography in a peripheral part of the body such as the forearms or legs and, in particular, the HR-pQCT (High-Resolution- peripheral quantitative computed tomography) that is a newly developed in vivo clinical imaging modality. It can assess the 3D microstructure of cortical and trabecular bone to evaluate bone's mechanical properties. (Liu, Saha, & Xu, 2012).

Fig.20- An example of p-QCT system

2.2.2.4. Single-photon emission computed tomography

Single-photon emission computed tomography (SPECT) is a method of computed tomography that uses radionuclides, which emit a single photon of a given energy. The camera is rotated 180 or 360 degrees around the patient to capture multiple 2-D images at multiple positions along the arc. A computer is then used to apply a <u>tomographic reconstruction</u> algorithm to the multiple projections, yielding a 3-D data set. It requires delivery of a gamma-emitting radioisotope administrated to the patient through injection into the bloodstream. It can be used to provide information about localised function in internal organs, such as functional cardiac or brain imaging, but at the same time, to complement any gamma imaging study such as thyroid imaging or bone scintigraphy. In some cases, a SPECT gamma scanner may be built to operate with a conventional CT scanner, with co-registration of images.

Fig.21 – SPECT Tomography

2.2.2.5. Positron emission tomography

Positron emission tomography (PET) is a nuclear medicine, functional imaging technique that observes metabolic processes in the body. It uses small amounts of radioactive materials called radiotracers, a special camera and a computer to help evaluate organ and tissue functions (Ziegler, 2005). It is used heavily in clinical oncology

(medical imaging of tumors and the search for metastases), but is also an important research tool to map normal human brain and heart function. PET scans are increasingly read alongside CT or magnetic resonance imaging (MRI) scans, because this combination (called "co-registration") provides both anatomic and metabolic information. PET imaging, in this way, became most useful; in fact, PET scanners are now available with integrated high-end multi-detector-row CT scanners (so-called "PET-CT").

Fig. 22 – PET Tomography

CHAPTER 3

Analysis of structural and densitometric parameters of bone

3.1 Osteoporosis

As mentioned in the Chapter 1, osteoporosis is the most common metabolic bone disease that affects the entire skeleton, particularly the cancellous and cortical bone. It occurs mainly in women going through menopause. In 2001, it was observed that 1 in 2 women and 1 in 5 men over age 50 in the West, would experience a fracture in their lifetime (Van Staa, Dennison, Leufkens, & Cooper, 2001). Current data are even more gruesome, in fact the National Osteoporosis Foundation (NOF) estimated that in 2010, 10 million Americans are to have osteoporosis and 34 million more to have low bone mass; furthermore is expected that the disease will increase to 14 million by 2020 (Cosman et al., 2014). For this reason, since 1994 the World Health Organization (WHO) reported that osteoporosis was a global problem and recommended bone mineral density (BMD) study for early detection of osteoporosis above all in the postmenopausal population.

Diagnosis of osteoporosis can be made thought radiographs when multiple fractures are present or when structural abnormalities, characteristic of the abovementioned disease, appear: in particular, low bone mass, micro-architectural deterioration of bone tissue and increased bone fragility. However, the use of visual observation and interpretation of a radiograph is not sufficient because technical considerations, such as patient size, exposure and processing factors, may be inaccurate and influence how dense the bones appear.

In the chapter 2 we saw that CT is an imaging technique that shows human anatomy in cross sections and provides a three-dimensional dataset that can be used for image reconstruction and analysis in distinct planes or three-dimensional settings. CT is used to provide not only morphological information, but also every information about tissue attenuation and to identify most of bone pathology, from traumatic lesions to bone neoplasm. Attenuation values can be extracted from CT data and used to reconstruct images. These values can also be used to estimate the density of tissues. (Celenk & Celenk, 2008).
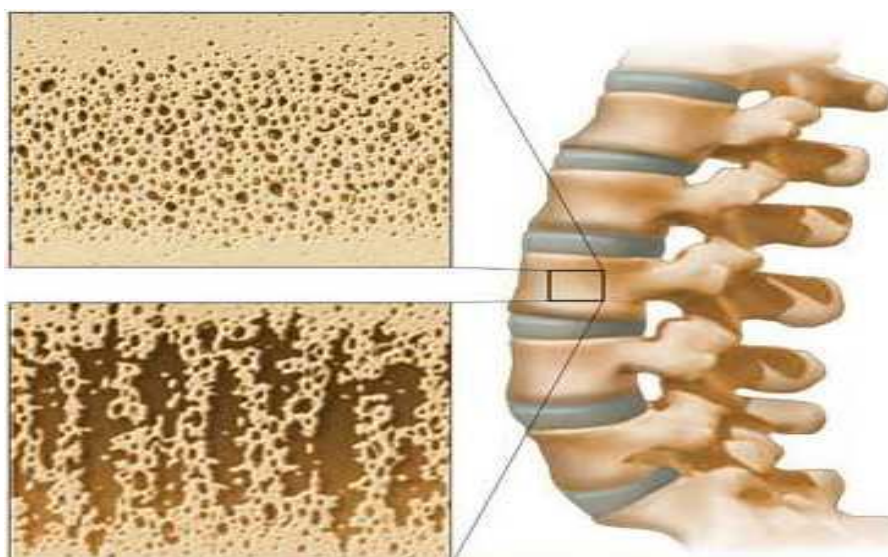
3.2 Bone Density

Bone density (or bone mineral density) is a medical term referring to the measure of mineral bone per square centimeter in a bone tissue (Fig.23). Bone density is used in clinical medicine as an indirect indicator of osteoporosis and fracture risk. BD measurements are most commonly made because the technique is non-invasive, painless and involves minimal radiation exposure. In recent studies, many approaches have been introduced to measure skeletal BD. All the methods for bone density measurement use a low-intensity beam of X-rays (or gamma-rays) passing through a patient and a radiation detector on the opposite side that quantifies how much of the beam is absorbed. Part of the beam is absorbed by the bone and part by the surrounding soft tissue. The purpose of each technique is to measure precisely how much is this difference. There are several types of bone mineral density tests such as:

- Ultrasound
- DEXA (Dual Energy X-ray Absorptiometry)

- SXA (single Energy X-ray Absorptiometry)

- PDXA (Peripheral Dual Energy X-ray Absorptiometry)

- RA (Radiographic Absorptiometry)

- DPA (Dual Photon Absorptiometry)

- SPA (Single Photon Absorptiometry)

- MRI (Magnetic Resonance Imaging)

- QCT (Quantitative Computed Tomography)

- Laboratory tests

QCT is considered as the gold standard compared with other measurements of Bone Density (Guglielmi, Grimston, Fischer, & Pacifici, 1994). Unlike the others, this technique produces a cross-sectional or 3-dimensional image from which the bone is measured directly, independently from the surrounding soft tissue. QCT, furthermore, allows to measure 100% isolated trabecular bone which is approximately eight times more metabolically active than cortical bone (Reinbold, Genant, Reiser, Harris, & Ettinger, 1986). Other techniques measure the mixture of trabecular bone and the overlying compact bone.

Fig. 23 – Difference between Normal Bone Density and Low Bone Density in a vertebra (“Bone Density Scan”).

3.3 Hounsfield Unit Scale

To quantify some property of the bone tissue, it is necessary to determine the standard calibration of the X-ray attenuation. For each pixel in an image, a numerical value (CT number) is assigned, which is the average of all the attenuation values contained within the corresponding voxel. This CT numbers are compared to the attenuation value of water and displayed on a scale of arbitrary units named Hounsfield units (HU) scale. In this way, it is possible to define the linear transformation of the original linear attenuation coefficient measurement into one in which the radiodensity of distilled water at standard pressure and temperature (STP) is defined as zero, while the radiodensity of air at STP is defined as -1000 HU (Celenk & Celenk, 2008).

For a material X with linear attenuation coefficient μ_x, the corresponding HU value is given by

$$HU = \frac{\mu_{x} - \mu_{water}}{\mu_{water} - \mu_{air}} \times 1000$$

Where μ_{water} and μ_{air} are respectively the linear attenuation coefficients of water and air. In Tab.1 the HU of common substances. It is important to underline that the Hounsfield number of a tissue varies according to the density of the tissue; so the higher the number, the denser is the tissue and the HU can be used directly to determine bone quality alterations.

Substance	HU
Air	−1000
Lung	−500
Fat	−100 to −50
Water	0
CSF	15
Kidney	30
Blood	+30 to +45
Muscle	+10 to +40
Grey matter	+37 to +45
White matter	+20 to +30
Liver	+40 to +60
Soft Tissue, Contrast	+100 to +300
Bone	+700 (cancellous bone) to +3000 (dense bone)

Tab.1 - A simple list of Hounsfield units for body tissues identified in a scan CT

The Hounsfield scale applies to simple X-ray CT scans, but not to cone beam computed tomography (CBCT) scans.

3.4 Structural parameters of bone

After scanning a specimen, having provided for its reconstruction and having established appropriate volume contours, it is possible, by suitably dedicated software, to provide information about the structural characterization of the bone tissue, carrying out in automatic the calculation of histomorphometric parameters.

Measurements, usually, are performed through particular known algorithms, which, in reference to the processing mode of the solid surface, can make use of the 2D model, or the 3D model. Some parameters can only be calculated by 2D or 3D methods; others can be calculated in both modalities. Parameter names follow two alternative

nomenclatures, "General Scientific" or "Bone ASBMR", the latter being based on a paper elaborated by Parfitt in the 1987. Parfitt's paper proposed a system of symbols for bone histomorphometry (Parfitt AM, Drezner MK, Glorieux FH, Kanis JA, Malluche H, Meunier PJ, Ott SM, 1987). All measurements of morphometric parameters in 3D and 2D are performed on segmented or binarized images. Segmentation, also called "thresholding", must be done prior to morphometric analysis (Skyscan, 2005). Following are some of the main parameters, classified according to nomenclature ASBMR, in reference to the bone tissue structure:

- **Total Volume (TV), (mm^3)**

  It represents the volume of interest, i.e. the total volume subjected to analysis, for the selected ROI (region of interest), including both the spaces occupied by bone material and the empty spaces. It can be measured both in 2D and in 3D and is based on a simple count of voxels contained in the selected volume model.

- **Bone Volume (BV), (mm^3)**

  It represents that part of the volume of interest occupied only by solid bone material; it can be calculated in 2D and 3D modes, and is based on counting voxel only recognized as a solid material.

- **Percent Bone Volume (BV/TV), (%)**

  It represents the percentage of the volume occupied by bone material compared to the total volume considered. It is calculated both in 2D and 3D, simply by making the ratio of BV and TV parameters, respectively calculated in two different ways.

- **Bone Surface (BS), (mm^2)**

  It represents the delimiting surface of regions occupied by solid bone material; the 2D measurement is based on surface " in steps", is therefore affected by inaccuracy due solely to processing perimeters of the cross sections; the measure in 3D is referred to the triangulated surface obtained by Marching Cubes algorithm.

- **Bone Specific Surface (BS/BV), (1/mm)**

  It represents the ratio between the surface and the volume of bone material; it is calculated in 2D and in 3D with reference to the BS and BV parameters obtained according to the two different modes.

- **Bone Surface Density (BS/TV), (mm/mm^2)**

  It represents the surface density that is the ratio between the surface area and the total volume of interest. It can be calculated in 2D and 3D, by performing the relationship of BS and TV parameters obtained according to the two different modes.

- **Trabecular Thickness (Tb.Th), (mm)**

  It represents the thickness of the trabeculae. It can be calculated in 2D and 3D. The calculation of this parameter by means of 2D analysis is carried out on the basis of some assumptions about the structural organization of the considered object; in this regard three different structural models can be used: a Parallel Plate Model, a Cylinder Rod Model and a Sphere Model. Using the Parallel Plate Model the trabecular thickness is calculated as

$$Tb.Th = 2\ \frac{BV}{BS}$$

With the Rod Cylinder Model the trabecular thickness is instead calculated as:

$$Tb.Th = 4\ \frac{BV}{BS}$$

Finally, with the hiring of the Sphere Model trabecular thickness is obtained from the relation:

$$Tb.Th = 6\ \frac{BV}{BS}$$

The 3D analysis instead allows to derive the parameter Tb.Th regardless of the model. The trabecular thickness is in fact defined as the average of all the local thicknesses across the voxels constituting the solid considered; the local thickness in a generic point of a solid is defined as the maximum diameter of the sphere that includes the point taken into consideration, not necessarily the geometric centre, and is entirely contained by a full volume. The software used provides the average value of Tb.Th for the entire sample (Hildebrand & Rüegsegger, 1997).

- **Trabecular Separation (Tb.Sp), (mm)**
  It represents the thickness of the interposed spaces between the trabeculae. It can be calculated with analysis in 2D and for that, it can be used the Parallel Plate Model, with which the trabecular thickness is obtained from the relation:

$$Tb.Sp = \frac{1}{Tb.N} - Tb.Th$$

or, with the Cylinder Rod Model, from the relation:

$$Tb.Sp = Tb.Th \cdot \left\{ \left[\left(\frac{4}{\pi} \right) \cdot \left(\frac{BV}{TV} \right) \right] - 1 \right\}$$

- **Trabecular Number (Tb.N), (1/mm)**

  It implies the number of traversals across a solid structure, such as a bone trabecula, made per unit length by a random linear path through the volume of interest (VOI). It is defined from the analysis in 2D using the Parallel Plate Model, according to the following relation:

$$Tb.N = \frac{BV}{TV} \cdot \frac{1}{Tb.Th}$$

while, with the Cylinder Rod Model:

$$Tb.N = \sqrt{\left[\left(\frac{4}{\pi} \right) \cdot \left(\frac{BV}{TV} \right) \right]} \cdot \frac{1}{Tb.Th}$$

Also in this case the difficulties of calculation introduced with the 2D analysis, are deleted by analysis performed directly in 3D. In this case, the trabecular number is defined by the same equation used for the calculation in 2D, with the assumption of a parallel plate model, with the important difference that the thickness of the trabecular bone is formed, not by means of the model, but through 3D analysis.

- **Structure Model Index, SMI**

  Structure model index indicates the relative prevalence of rods and plates in a 3D structure such as trabecular bone. SMI involves a measurement of surface convexity. This parameter is of importance in osteoporotic degradation of trabecular bone, which is characterised by a transition from plate-like to rod-like architecture. An ideal plate, cylinder and sphere have SMI values of 0, 3 and 4 respectively (Skyscan, 2005). The SMI calculation is based on dilation of the 3D voxel model, that is, artificially adding one voxel thickness to all digitised object surfaces (Hildebrand & Rüegsegger, 1997).

$$SMI = 6 \cdot \frac{(S' \cdot V)}{(S^2)}$$

  where V is the initial volume of the object, S is the area of the object surface before the dilatation, S 'the variation of surface after dilation.

- **Mean Intercept Length, MIL**

  Mean intercept length analysis measures isotropy. It is found by sending various line, forming an equispaced grid with an orientation Ө, through a three-dimensional image volume containing binarized objects, and counting the number of intersections I between the grid and the bone-marrow interface. Note that in this MIL calculation the intercept length may correlate with object thickness in a given orientation but does not measure it directly.

$$\text{MIL } (\Theta) = \frac{L}{I(\Theta)}$$

where L is the total line length.

In the Fig.24 is shown an example of the grid of lines that formed through the volume over a large number of 3D angles; in this case only two of them. The MIL for each angle is calculated as the average for all the lines of the grid.

- **Degree of anisotropy, DA**

  Isotropy is a measure of 3D symmetry. Anisotropy, opposed to isotropy, is a term used when properties of the matter are not the same when measured from any direction. In the case of an anisotropic structure, the plot of MIL gives an ellipsoid, in which the principal axes represent the main trabecular orientation. The ratio between the lengths of the principal axes gives an information about the anisotropy of the structure, i.e. the degree of anisotropy (Goulet et al., 1994).

$$DA = \frac{\max MIL}{\min MIL}$$

Traditionally, the value of the degree of anisotropy are 1 when the structure is fully isotropic and 0 when is fully anisotropic.
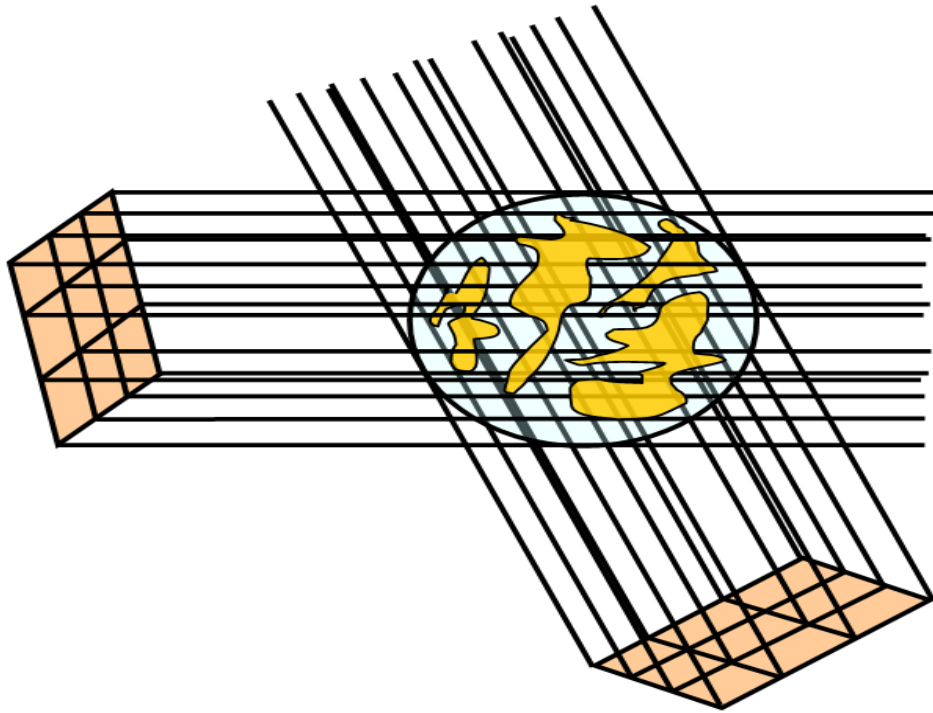
Fig. 24 – A 3D representation for the MIL calculation (Skyscan, 2005)

- **Connectivity**

  Connectivity is defined as a measure of the degree to which a structure is multiple connected per unit volume (Odgaard, 1997). Thus, for a network, it reports the maximal number of branches that can be broken, before the structure is separated in two parts. Trabecular bone is one such network, and its connectivity density (Conn.D) can be calculated by dividing the connectivity estimate by the volume of the sample; this is very important because trabecular connectivity can contribute significantly to structure strength. To provide a measure of connectivity density, it resorts to the use of Euler analysis and in particular, with Euler number, which components are constituted by the three Betti numbers.

$$X(x) = \mathcal{B}_0 - \mathcal{B}_1 + \mathcal{B}_2$$

This is the Euler-Poincaré formula for a three-dimensional object, where $\mathcal{B}_0$ is the number of objects, $\mathcal{B}_1$ is the connectivity, and $\mathcal{B}_2$ is the number of enclosed cavities.

- **Total Porosity, (%)**

  Total porosity is the volume of all open plus closed pores as a percent of the total VOI volume. A closed pore in 3D is a connected aggregation of space (black) voxels that is surrounded on all sides in 3D by solid (white) voxels. An open pore is defined as any space located within a solid object or between solid objects, which has any connection in 3D to the s pace outside the object or objects (Skyscan, 2005).

3.5 Bone Quality

Usually, a fracture occurs when the external force applied to a bone exceeds its strength. Whether or not a bone will be able to resist the fracture depends by many factors such as the amount of bone present, the spatial distribution of the bone mass, the microarchitecture, the composition of bone matrix and the intrinsic properties of each of the bone components.

The calculation of the micro-architectural parameters of bone structure above mentioned, mostly in the trabecular bone, has proven, over the years of scientific research, to be more useful in evaluation of bone quality and in distinguishing between patients with and without osteoporotic fractures (Guglielmi, 2010).

Bone quality describes aspects of bone composition and structure that contribute to bone strength independently from bone mineral density; Alterations in bone microarchitecture make an important contribution

to bone strength. For example, in cancellous bone, important support is given by the size, the shape and the connectivity of trabeculae, whilst in cortical bone cortical width, cortical porosity and bone size are the major benchmarks (Compston, 2006). New techniques are being developed to assess the risk of fracture, evaluate new therapies and predict implant success: all of them require specific measurements of local bone micromechanical properties.

CHAPTER 4

Experimental tests at the Laboratory of Medical Technology of "Rizzoli Orthopedic Institute"

4.1 Aim of the thesis

The aim of this work done at the Laboratory of Medical Technology at the Rizzoli Orthopedic Institute is to compare, through two methods of tomographic imaging (micro-CT and Cone Beam CT), the morpho-structural parameters characterizing the bone tissue and, in greater depth, the trabecular component. In particular, the two available procedures make it possible to have scans at different resolutions: defined the first one as the reference standard as able to produce higher spatial resolutions (although applicable only in-vitro), the intent is to investigate if and how the structural parameters concerning the bone tissue could also be estimated from the second (applicable in-vivo), that has different characteristics given not only by a lower resolution but also by alteration of tissue information derived from it.

The study, in addition, also tackles the problem of the determination of the optimal thresholds for the images binarization. The obtained images will allow, by the appropriate software, the calculations of histo-morphometric parameters.

4.2 State of the art

Many studies in the literature evaluate the comparison between the two imaging methods examined in my thesis. Quantitative bone

morphometry is the standard method to assess structural properties of trabeculae by means of morphometric indices.(Parfitt AM, Drezner MK, Glorieux FH, Kanis JA, Malluche H, Meunier PJ, Ott SM, 1987). In the past, microarchitectural characteristics of trabecular and cortical bone have been intensively investigated by examining two-dimensional (2D) sections of bone biopsies, combined with calculation of morphometric parameters using stereological method. To overcome some of the limitations of 2D analyses, various three-dimensional (3D) imaging modalities have been proposed.

Most of the studies concerning the comparison between micro-CT and CBCT are made in dentistry and maxillofacial investigations, using mainly bone samples from cadavers of animals. In fact, cone beam computed tomography (CBCT) was developed and applied above all to presurgical imaging for dental implant treatment (Naitoh, Aimiya, Hirukawa, & Ariji, 2010). To establish CBCT as a method for 3D assessment and analysis of trabecular bone, the method needs proper validation by comparing the results with 3D µCT, serving as the reference (gold standard). During the last decade, various advancements within the CBCT imaging chain have led to clear improvements in resolution. However, spatial resolution is highly variable between CBCT devices, with voxel sizes between 76 µm and 400 µm. A previous study has shown that images with voxel sizes higher than 300 µm would be unsuitable for imaging individual trabeculae. (Issever et al., 2010). With the time, many steps have been made: the accuracy of cone beam CT in measuring the trabecular bone microstructure in comparison with micro-CT, was determined also with a study of human mandibular bone samples (J Van Dessel, Y Huang, M Depypere, I Rubira-Bullen, 2013), which has demonstrated the potential of high-resolution CBCT imaging for *in-vivo* applications of

quantitative bone morphometry and bone quality assessment. High positive Pearson's correlation coefficients were observed between CBCT and micro-CT protocols for all tested morphometric indices except for trabecular thickness. However, the overestimation of morphometric parameters and acquisition settings in CBCT must be taken into account. A similar study, evaluating at dental implant site with the methods abovementioned, was done (Parsa, Ibrahim, Hassan, van der Stelt, & Wismeijer, 2015) and the obtained results confirmed a strong correlation between CBCT grey values and those of micro-CT, suggesting the potential of this modality in bone quality assessment.

4.3 Materials and Methods

4.3.1 Bone Samples

The study is organized into three main phases, in which three different types of bone tissue samples are analyzed, with structures of increasing complexity. In detail:

- **Sample type 1**: 5 cylindrical biopsies from femoral (Fig. 25) bone of cadavers with a height of 3 cm and a diameter of 1.1 cm, characterized by only trabecular tissue.

- **Sample type 2**: 3 biopsies from tibial bone (Fig.26) of cadavers characterized mainly by cortical tissue; in this case, the specimen's height is 4.5 cm and the diameter is 3.6 cm.

- **Sample type 3**: 17 thoracic and lumbar vertebrae (Fig.27) of cadavers with both trabecular and cortical bone.

Sample type 1. The samples were selected as having 5 different values of BV/TV (%): Specimen 1 with BV/TV about 12 %, Specimen 2 with BV/TV about 20%, Specimen 3 with BV/TV about 6%, Specimen 4 with BV/TV about 16% and Specimen 5 with BV/TV about 25%.

They were previously embedded in PMMA (Polymethyl-methacrylate), a synthetic polymer of methyl methacrylate: this is a very adaptable material used in various application fields including the biomedical sector. Used to preserve the specimen in the course of time and, given its extreme biocompatibility, it is resistant to long exposure to different temperatures and chemical agents. In orthopedic surgery, PMMA is known as bone cement, and is used to fill the space between implant and bone. The most important aspect for the use of PMMA is that it has a mass attenuation coefficient which is similar to water and soft tissue (at 30 keV: μPMMA= 0.36 cm-1, μWater= 0.38 cm-1) (Hubbell & Seltzer, 1995). For this reason, in particular, the bone is included with something that has similar characteristics as soft tissues.

Sample type 2. Also these samples were embedded in PMMA to better simulate the ideal condition of bone stability. There aren't enough information about the samples origin.
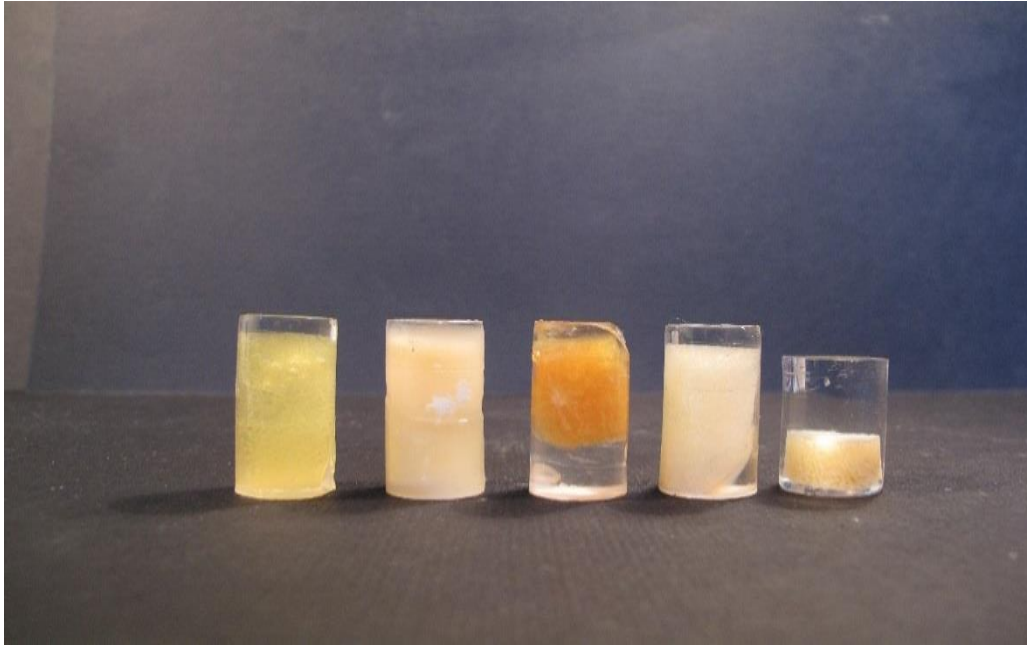
Fig.25 – Five cylindrical biopsies from femoral bone of cadavers. Rif. "Laboratory of Medical Technology of "Rizzoli Orthopedic Institute"

Fig.26 – 3 biopsies from Tibial Bone of cadavers. Ref."Laboratory of Medical Technology of "Rizzoli Orthopedic Institute"

Sample type 3. The vertebrae in exam (Fig.27) belonged to individuals of African and Caucasian origin of both sexes aged between 68 and 79 years who had been diagnosed with an important form of osteoporosis.

Fig. 27 – Thoracic vertebrae of cadavers. Ref. "Rizzoli Orthopedic Institute

4.3.2 Tomographic Imaging Methods

In this thesis, attention focuses mainly on two widely used imaging techniques, working with different spatial resolutions: micro-CT and CBCT (cone beam CT).

Specifically, two micro-CT devices are available for scientific research at the Rizzoli Orthopedic Institute, in Bologna. The first one is a BRUKER SkyScan 1072 (Skyscan, Aartselaar, Belgium) (Fig. 28) and the second one is a BRUKER SkyScan 1176 (Skyscan, Aartselaar, Belgium) (Fig. 29). SkyScan 1072 is used for in-vitro imaging while SkyScan 1176, besides the application in-vitro, has also a high performance in-vivo for preclinical research on small laboratory animals. Both the systems have a very high spatial resolution power, of the order of few µm (www.skyscan.be).

Micro-CT SkyScan 1072 (Fig.28) is characterized by an X-ray microfocus tube with high-voltage power supply, a specimen stage with precision manipulator, a two-dimensional X-ray CCD-camera connected to the frame-grabber and a computer with a colour monitor.

The X-ray source is a 10 W microfocus tube (tungsten), which can operate at currents and voltages up to 98 μA and 100 kVp respectively. The cone beam geometry allows an optical magnification of the object in examination on the detector system. Depending on the chosen magnification, the field of view (FOV) can range from 20 mm to 2 mm with a nominal isotropic spatial resolution ranging from about 20 μm/pixel to 2 μm/pixel, respectively. The special X-ray CCD camera is based on high resolution (1024x1024 pixels) cooled CCD sensor with fibre optic coupling (3.7:1 image reduction) to X-ray scintillator or 768x560 pixels CCD sensor with lens coupling to X-ray scintillator.

The system is supplied with a 1 mm-thick aluminium plate, which can be used as hardware filter for minimizing beam hardening, by placing it in front of the scintillator.


Fig.28 MICRO-CT SkyScan 1072 in use at Laboratory of Medical Technology of "Rizzoli Orthopedic Institute"

Micro-CT SkyScan 1176 (Fig.29) has instead an X-ray microfocus tube that operates in the range 20-90kVp, with a maximum power of 25W. The special X-ray CCD-camera is based on 11 Megapixel (4000x2672 pixels) cooled CCD-sensor with fibre optic coupling to the X-ray scintillator. The scanning area is 68mm x 200mm or 35mm x 200mm. It is based on spiral scan to avoid ring artefacts and partial scan connections and the time for a full scanning cycle is less than 1 minute (1Kx1K slice format). The minimum pixel size is 9 μm and the low-contrast spatial resolutions is equal to 15 μm (10% MTF). The "bed" on which to place the samples or the animals is available in carbon fiber or polystyrene foam and it is integrated with a physiological monitoring subsystem that provides breathing and heart-beat gating for proven thoracic image improvement by synchronized acquisition ("www.bruker.com," n.d.).
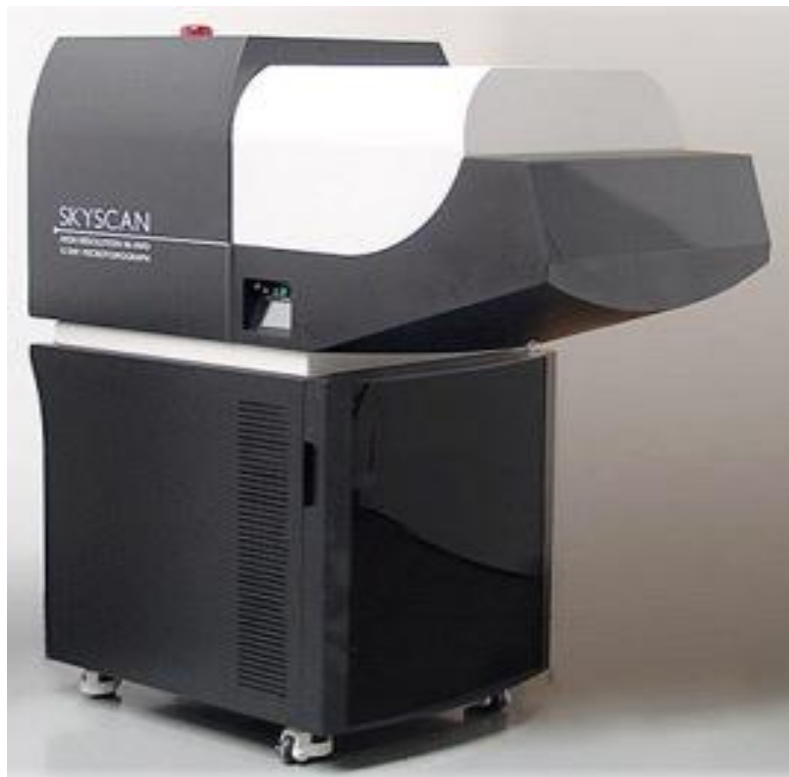
Fig.29 – Micro-CT SkyScan 1176 in use at the "Rizzoli Orthopedic Institute"

As regards the Cone Beam CT diagnostic technique, scans were performed with the use of a device produced by the manufacturer QR SRL (hereinafter QR) based in via Silvestrini, 20, Verona (Italy). The CBCT device is precisely the **Cone Beam CT 3D NewTom 5G** (Fig.30), which, with spacious gantry and motorized bed, is capable of scanning various anatomical areas of the body ("www.newtom.it," n.d.). The main features of the machine are the following: X-ray source, with rotating anode, maximum voltage 110 kVp; 1-20 mA (pulsed mode), focal spot of 0.3mm, scan time in the range 18-36s; it takes an image at every degree of rotation that is of 360°. The image detector is an amorphous silicon flat panel, with a 20 cm x 25 cm Field of View. Cone Beam 3D imaging uses a cone-shaped beam to acquire the entire image of the object in a single scan using only one rotation. It is mostly applied for dental and maxillofacial investigations.
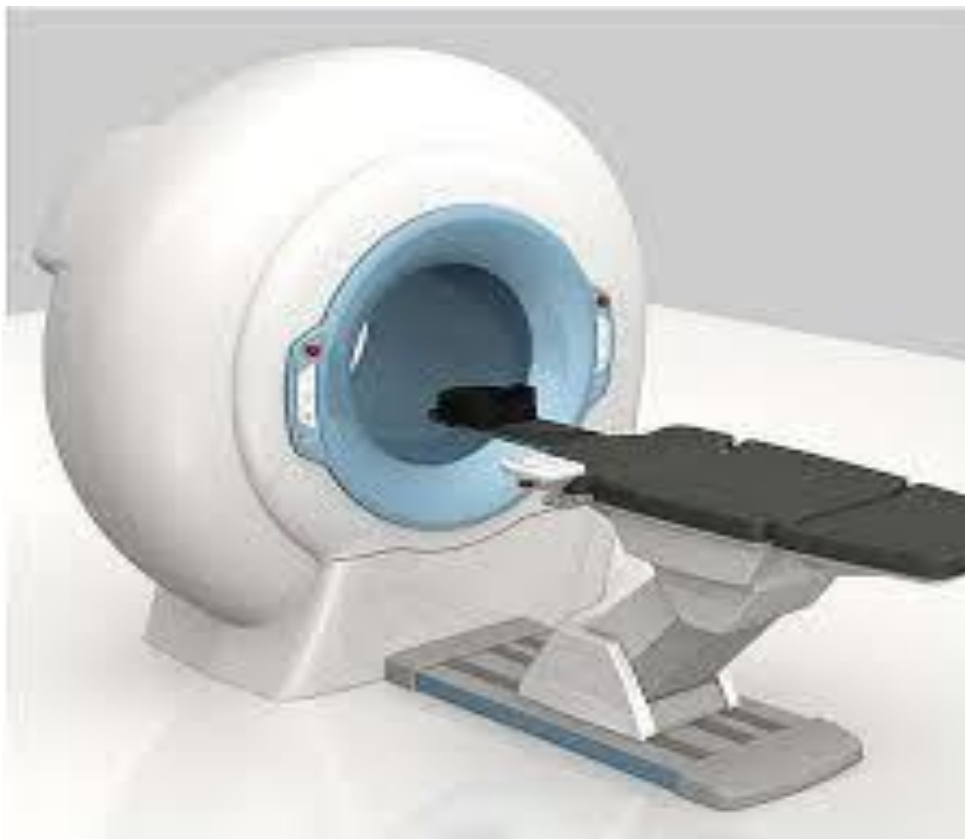

Fig. 30 – CBCT 3D NewTom 5G machine. Ref. www.newtom.it

4.3.3 Image Acquisition

For each sample abovementioned, scanning and subsequent comparison was performed using different devices. The samples of group 1 were scanned by micro-CT method using the device SkyScan 1176. Cone Beam CT acquisition were done by using two different Newton 5G devices. The first one was located at the "Spedali Civili" in Brescia in collaboration with the "Medical Physics Unit"; the second one was located at the "QR" of Verona, in collaboration with the "Imaging Department". The source of micro-CT SkyScan 1176 has been set at 80 kVp, 313 µA, using the 1 mm-Al filter for beam hardening minimization. The exposure was fixed at 66 µs, the rotation step at 0.300 deg, smoothing at 1, ring artifact correction at 7 and image pixel size at 34.95 µm.

The parameters set for the CBCT scans have been set at 110KVp with an exposure time of 15s and image pixel size at 100 µm.Figures 31a and 31b show a frontal X-ray projection of one of the cylindrical cancellous bone biopsies of femoral bone of a cadaver, obtained with SkyScan 1176 (a) and Cone Beam CT Newtom 5G (b) respectively.
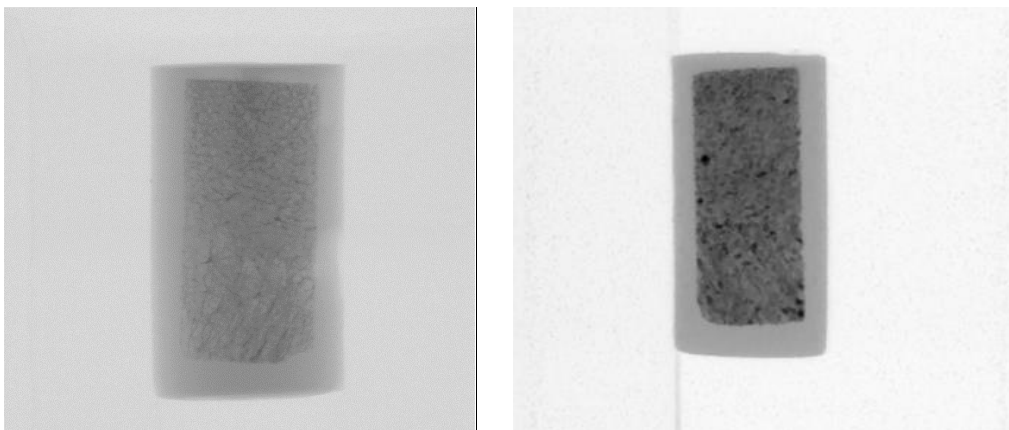
Fig 31- Frontal X-ray projection obtained by means of micro-CT SkyScan 1176(a) and CBCT Newton 5G(b) of a cylindrical bone biopsy with a image pixel size of 34,95 µm and 100 µm respectivily. Ref. Laboratory of Medical Technology at "Rizzoli Orthopedic Institute".

The specimens of group 2 were scanned by micro-CT method using the SkyScan 1176 device and by Cone Beam CT using the Newton 5G machine in use at the "Spedali Civili" in Brescia with the same acquisition parameters of "sample type 1". In this case, the datasets obtained from the scans were subjected in advance to an operation called "3D Registration" by means of the Software DataViewer (Bruker, Belgium) so that the dataset selected as "target" is transformed into the coordinate system of the dataset selected as "reference" which stays stationary. More information about the Image Registration can be found below.

The samples of group 3 were scanned with SkyScan 1176 and with Newtom 5G in use at QR of Verona. Also in this case, the acquisition parameters are the same used for the previous groups of samples. The only difference in the scanning of the objects is that, while the samples of groups 1 and 2 were scanned embedded in PMMA, the third type of samples was scanned in air, wrapped in a layer of parafilm, an efficient laboratory material, that with its high elasticity, guarantees optimal fit and protects against evaporation, contamination and hydration. The specimens were placed on the machine's bed with their main transverse axis parallel to that of the bed itself (in order to avoid reaching the limits of the field of view where it has the more evident artifacts with increasing resolution). Also in this case, the datasets scanned with two different techniques, are "registered" to ensure that the images have the same three-dimensional reference system.

4.3.4 Image Reconstruction

The reconstruction operation allows tracing information on the intensity of beams attenuated in all directions and on the linear attenuation

coefficient relative to each volume element. The reconstruction of the microtomographic images was performed by means of a special software, provided by the home manufacturer of the device, the SkyScan NRecon (Bruker, Belgium), in which the process is based on a particular type of Feldkamp algorithm. The Feldkamp algorithm is the most used for the reconstruction of images obtained with cone beam tomography; it is based on the Radon transform, the mathematical tool which ensures the reconstruction of an object from its projections. The obtained images can be saved in different file formats; in this case, the 8-bit BMP format was chosen.

The output images from Cone Beam CT are DICOM images, a standard and public format, now used in the vast majority of biomedical products especially in the field of radiology.

4.3.5 Image Registration

For the samples of groups 2 and 3, it was necessary to apply the Image Registration, in order to convert different sets of data into one coordinate system. It is a recurring problem in the medical imaging, as it is not possible to have a precise standardization of the scanning process when the same subject is scanned in different times or even with different tomographic methods. In this case, two different approaches depending on the considered sample are used. In fact, for sample of group 2 it was enough to use the software DataViewer (Bruker) to record the various data sets of images (Fig.32).
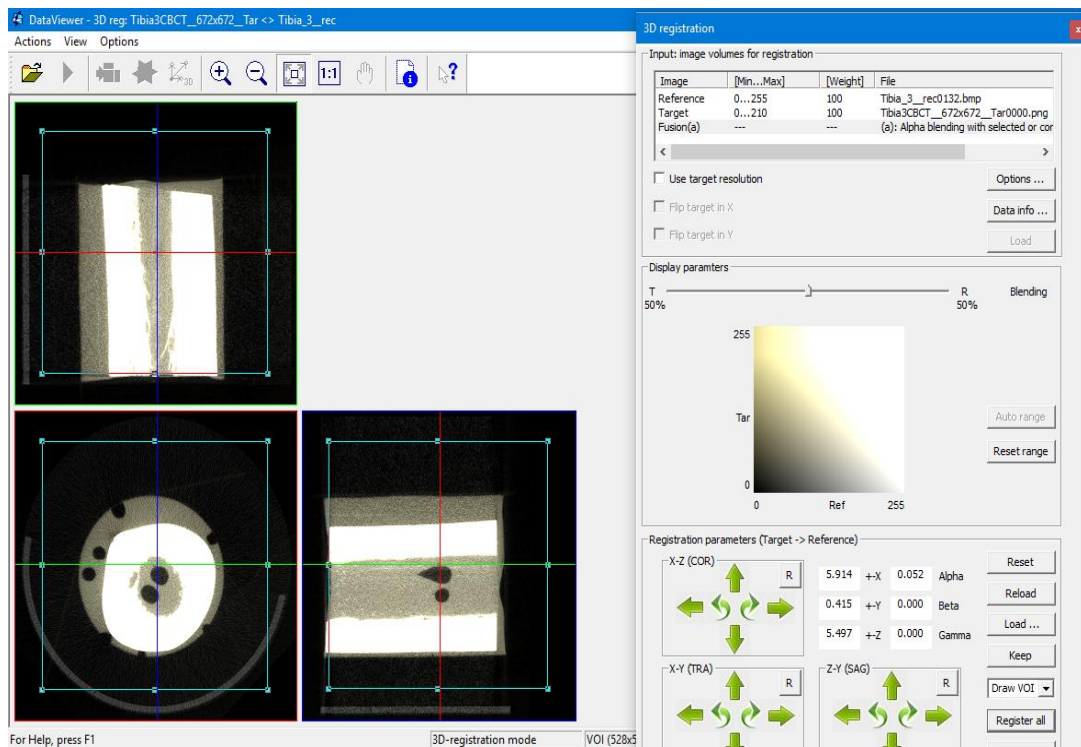
Fig.32- An example of "3D Registration" function using DataViewer software. The dataset selected as "target" is transformed into the coordinate system of the dataset selected as "reference"

Once a reference and a target datasets have been set, the target is transformed into the coordinate system of the reference that stays stationary.

For sample of group 3, instead, the registration process was much more laborious. DataViewer becomes efficient only for "small displacements" and only if the datasets have been scanned in the same way in the three axes of reference x, y, z. Conversely, the vertebrae location varied from time to time in the two methods of scanning; for this reason, the procedure was divided into several steps:

- converting images from BMP format to VTK format so that it could be created, using the 3D graphics program *ITK – SNAP*, an STL file that describes a raw unstructured triangulated surface by the unit normal and vertices (ordered by the right-hand rule) of the triangles using a three-dimensional Cartesian coordinate system. STL

62

coordinates must be positive numbers, there is no scale information, and the units are arbitrary (Fig.33). Starting from it and from all the slices related to the volume of interest of the sample (for each one), it was reconstructed the three-dimensional image of the vertebra (Fig. 34)

- manual roto-translation operations of the obtained 3D surfaces through *BUILDER* software (free available at www.bonemat.com) to obtain the corresponding matrix of rotational translation

- ad hoc optimization of that matrix with the use of *MatLab* scripts (Matlab, The Mathworks Inc, Natick, MA,USA), which provide the registration of an STL surface 'moving' on a STL surface 'target'.

- calculation of the Euler angles that describe the orientation of a rigid body and in particular, the orientation of a coordinate system relative to another.

- registration of a dataset in the other reference system in which micro-CT dataset was defined as target and CBCT dataset as moving.
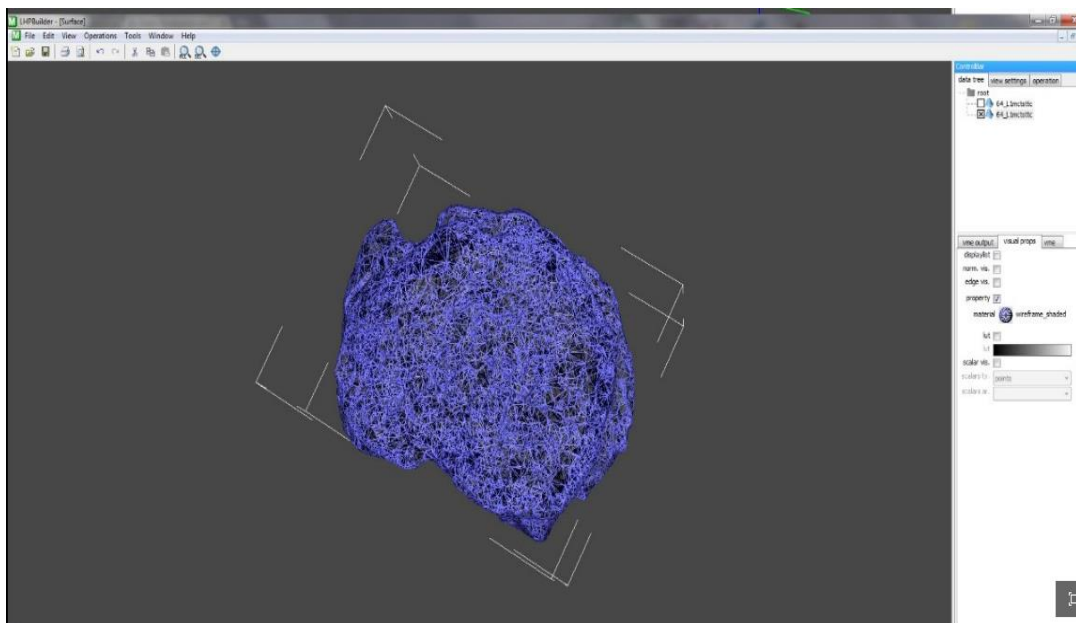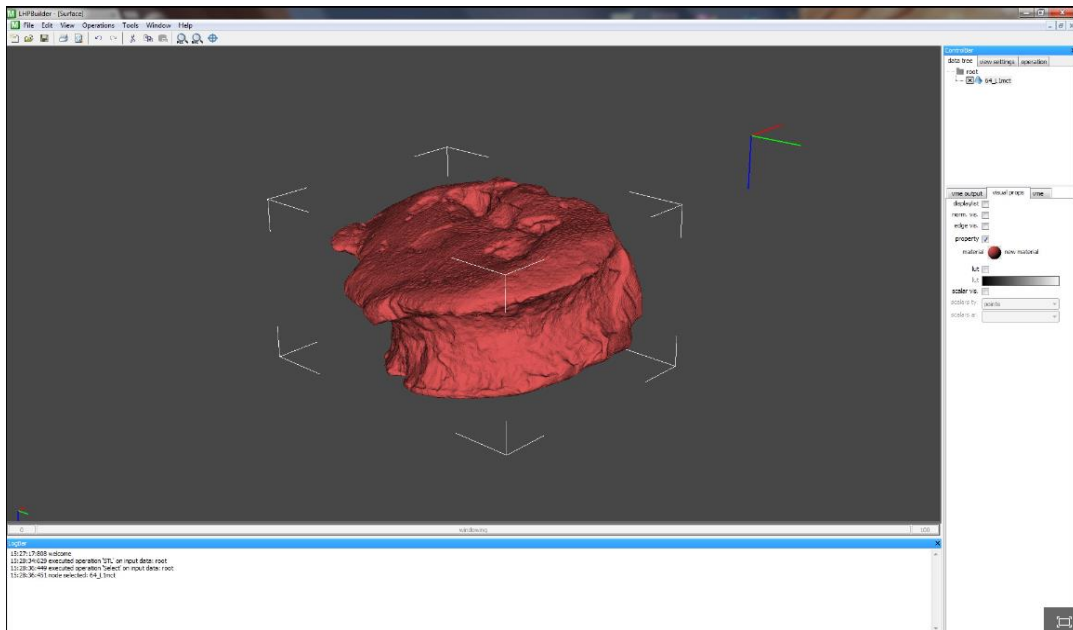

Fig.33 – STL surface of a vertebra

Fig. 34 – Three-dimensional image of the vertebra reconstructed from STL surface

4.3.6 Validation of an optimal threshold for image segmentation

Before proceeding with calculation of the histomorphometric parameters, the grey level image has to be previously segmented into a bone and non-bone phase. This process, also called "segmentation", "thresholding" or "binarization", has as a result an image composed only of black or white pixel, where black means non-bone while white means bone.

First of all, it was appropriate to define a threshold value for the micro-CT SkyScan 1176; in the absence of comparisons with the "real" histological value of the samples, it was proceeded with the validation of an "optimal thresholding" using the cross comparison with the acquisitions on SkyScan 1072 of 5 samples of trabecular bone included in PMMA at disposal, with BV/TV values between 6 and 25 % (the same specimens previously identified as sample type 1). The scans of these samples on the SkyScan 1176, conducted with the same

acquisition parameters, were analyzed with variable thresholds (about 100 thresholds for each specimen) up to replicate the BV/TV values acquired on SkyScan 1072 with the trabecular bone protocol. The used method was the *Minimum Variation* of the parameter in question: for example, for BV/TV parameter, the change in bone volume fraction (BV/TV) in relation to the threshold value was investigated; then, the value corresponding to the minimum variation of BV/TV parameter variation, was selected as the global threshold value (Ding, Odgaard, & Hvid, 1999).

The same mechanism was used to identify the optimal "threshold" for the elaboration of the tomographic images from Cone Beam CT Newtom 5G taking, as a reference, the threshold value previously obtained from micro-CT SkyScan 1176.

For the sample of the group 2, the validation of an optimal threshold has been performed in a different way because the protocol used above, is applicable mostly in samples characterized by trabecular tissue. For cortical tissue, instead, a technique has been used where a single threshold value is selected, based on the distribution of the gray levels in the images. The histogram of these images, in fact has two rather obvious peaks, corresponding to the bone material (lowest peak) and the background (highest peak); the optimal threshold is therefore identified in the minimum point between the two peaks.


4.3.7 Image Segmentation and Calculation of the Histomorphometric Parameters

Through the software released by the Bruker manufacturer (SkyScan, Belgium), *Ct–Analyser*, first the identification of a Region of Interest (ROI) was done in order to perform 3D calculations. Specifically, for

the sample of the group 1, a circle ROI of 9 mm was defined, interpolating it over the whole dataset taken into account. For the sample types 2 and 3, a manually defined polygonal ROI was chosen, in order to select the trabecular tissue. In the first case, accurate attention has been paid to identify only cortical tissue; conversely, in the second case the vertebrae have been "cleaned" ad hoc from cortical bone tissue to select only trabecular tissue. Subsequently, with the defined threshold, the image binarization was carried out. The pictures below show an example of cross-sectional image for each group of samples and the corresponding segmented images, obtained with micro-CT (Fig.35) and Cone Beam CT (Fig.36) scanners, respectively.

With global threshold, the histomorphometric parameters discussed above were estimated over a selected volume of interest (VOI) of micro-CT slices for each specimen. The volume of interest is chosen taking the greatest possible number of slices. For trabecular bone, the attention was focused on the BV/TV (%), Tb.Th (mm) and Tb.Sp (mm). For the cortical bone analysis, instead, the calculations involved DA and Total Porosity (%).
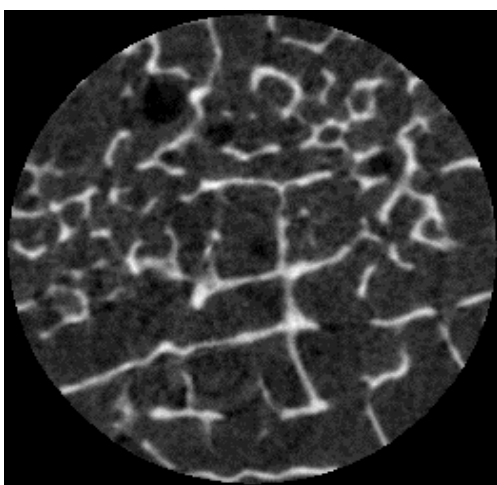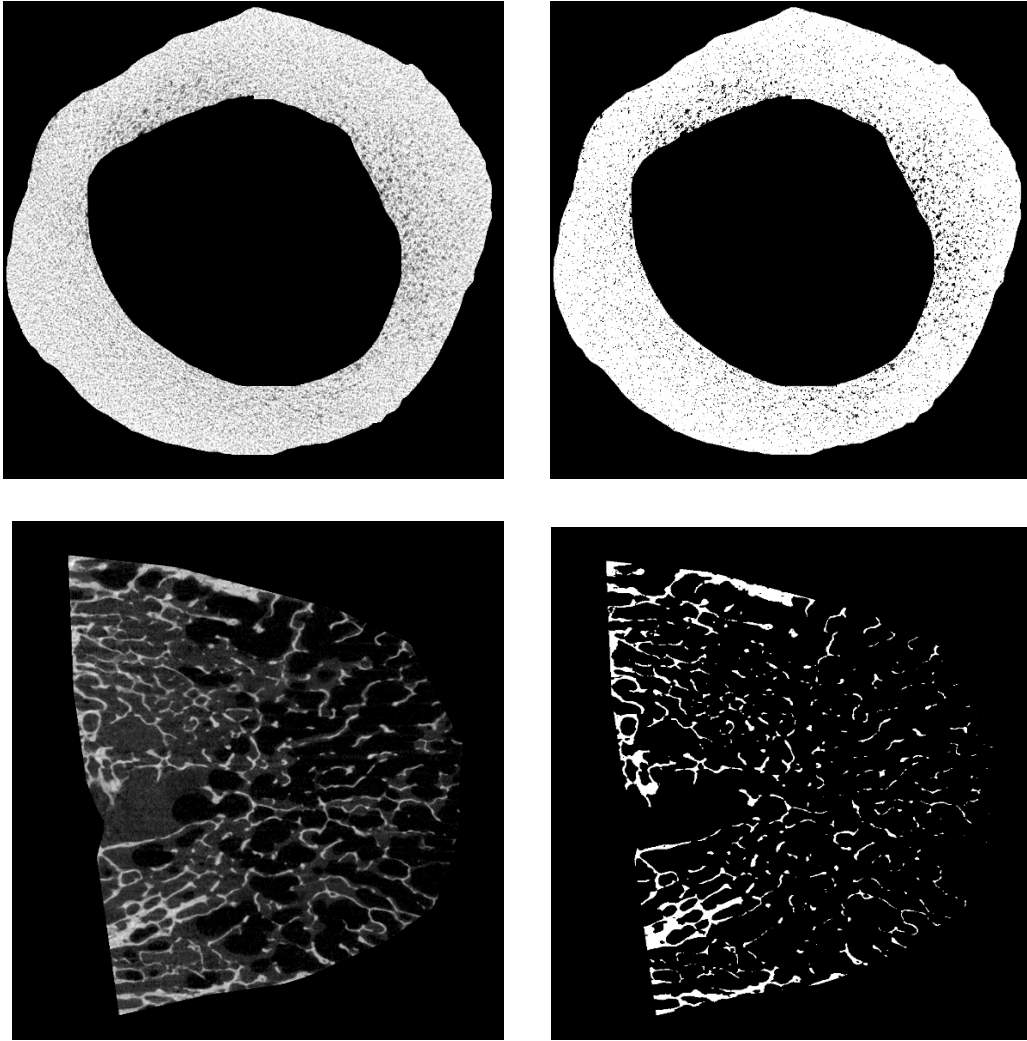
Fig. 35 - Cross-sections and corresponding segmented images obtained with micro-CT scanner SkyScan 1176 and Ct-Analyser Software. Ref. Laboratory of Medical Technology at the "Rizzoli Orthopedic Institute"
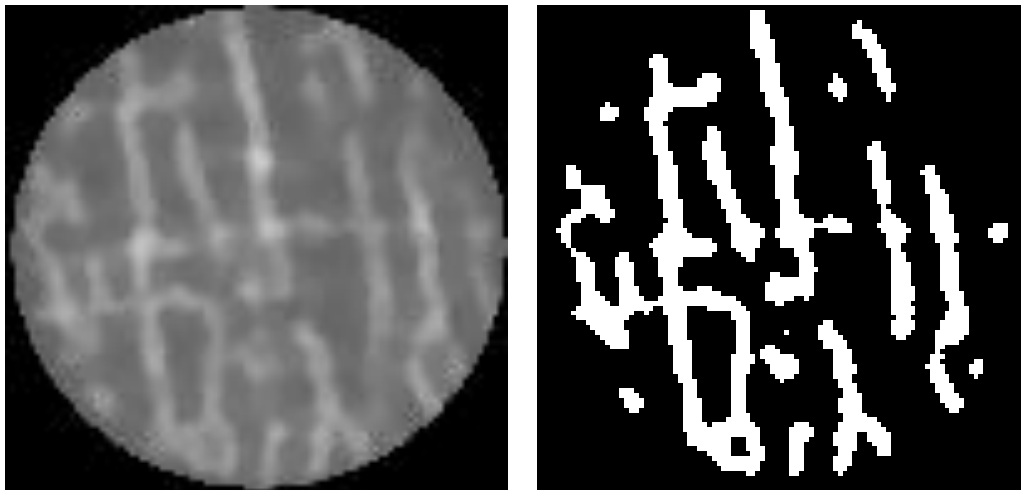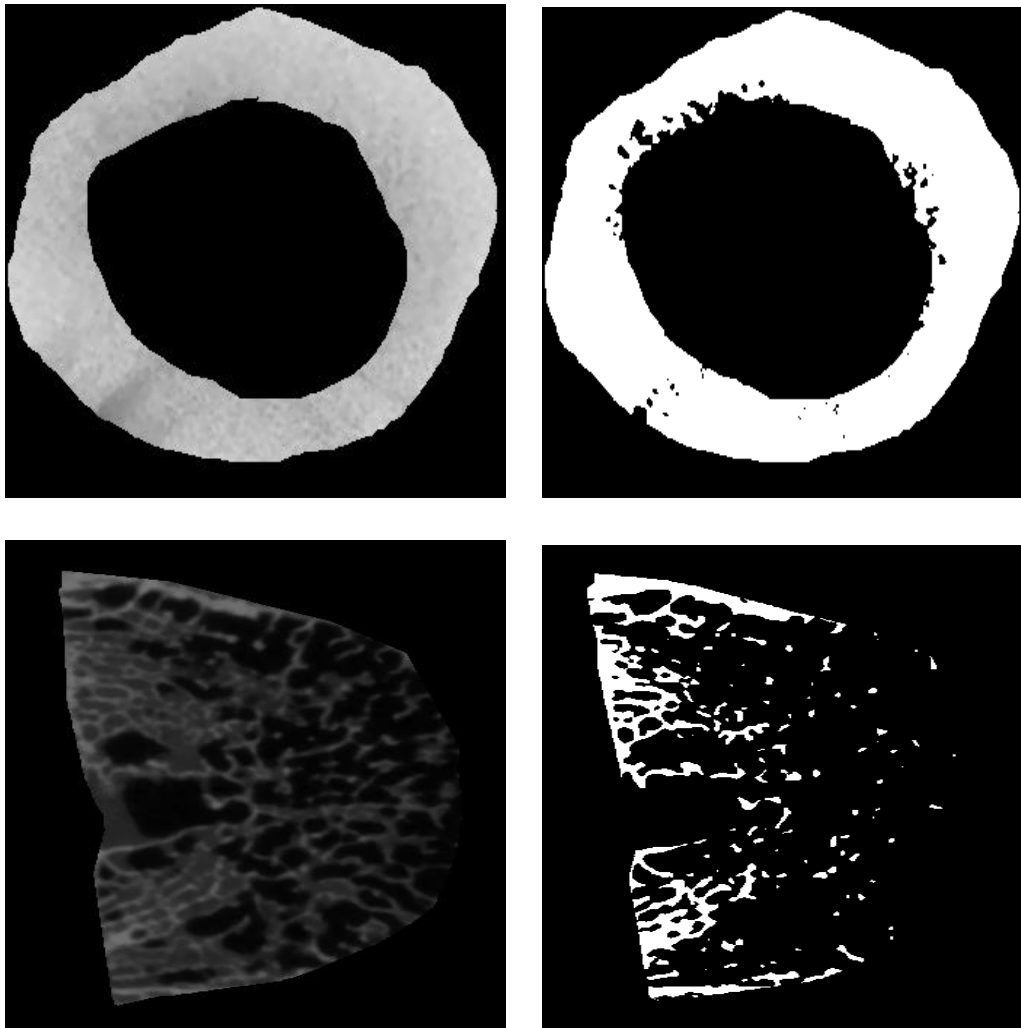
Fig. 36 - Cross-section and corresponding segmented images obtained with scanner Cone Beam CT 5G and Ct-Analyser Software. Ref. Laboratory of Medical Technology at the "Rizzoli Orthopedic Institute"

4.4 Statistical Analysis

The correlation between different methods was analyzed by using the Linear Regression Model.

Linear regression is the most basic and commonly used predictive analysis. Regression estimates are used to describe data and to explain the relationship between one dependent variable and one or more independent variables. At the core of the regression analysis is the task

of fitting a single line through a scatter plot. The simplest form with one dependent and one independent variable is defined by the formula

$$y = c + b*x$$

where y is the estimated dependent variable, c is a constant, b is the regression coefficient and x is the independent variable. Linear regression analysis consists of more than just fitting a linear line through a cloud of data points, it consists of 3 particular stages: analyzing the correlation and directionality of the data, estimating the model, i.e., fitting the line, and evaluating the validity and usefulness of the model. Adding independent variables to a linear regression model will always increase the explained variance of the model (typically expressed as R^2).

R^2, the *coefficient of determination*, is a number that indicates the proportion of the variance in the dependent variable that is predictable from the independent variable, it gives some information about the goodness of fit of a model because it is a measure of how well the regression line approximates the real data points. An R^2 of 1 indicates that the regression line perfectly fits the data, while values of R^2 close to zero may occur when fitting non-linear functions to data.

CHAPTER 5

Analysis of Results

In this chapter, the results of all measurements taken on the three different groups of samples are described and analyzed.

5.1 Defining the optimal threshold value for SkyScan 1176 micro-CT scanner

As mentioned in the Chapter 4, before proceeding to the segmentation of the images and to the relative calculation of the structural parameters, it was appropriate to define a threshold value for elaboration of the images obtained by means of the SkyScan 1176 micro-CT scanner. For this purpose, in the absence of comparison with the parameters calculated histologically, the method of *Minimum Variation* was used as previously explained. The comparison was based on the knowledge of the optimal threshold for the segmentation of images obtained with SkyScan 1072, calculated in a previous study carried out at the Medical Technology Laboratory of Rizzoli Orthopedic Institute by using the same specimens of group 1. The threshold calculated for SkyScan 1072 is equal to 117 in a scale of 256 gray-levels. Through the calculation of Minimum Variation, the threshold identified as "optimal" for the segmentation of images obtained by the SkyScan 1176 amounted to **123**.

The functional relationship between the variables was evaluated through the simple *Linear Regression Model* calculating the coefficient of determination to estimate the proportion between the variability of the data and the correctness of the employed statistical model.

Table 2 below, contains the BV/TV (%) values calculated from the microtomographic images obtained with SkyScan 1072 and SkyScan 1176 with both devices at different thresholds (117 and 123 respectively) and the corresponding Linear Regression Model (Fig. 37).

SAMPLE TYPE 1	BV/TV (%) SkyScan 1072	BV/TV (%) SkyScan 1176
Specimen 1	12,4±0,3	12,4±0,9
Specimen2	20,0±0,5	21,3±1,6
Specimen 3	7,14±0,17	6,5±0,5
Specimen4	16,8±0,4	18,1±1,3
Specimen 5	25,4±0,6	28,2±2,1

Tab. 2 – Values of BV/TV (%) calculated from the microtomographic images of the first group of samples, obtained with SkyScan 1072 (threshold value equal to 117) SkyScan 1176 (threshold value equal to 123).
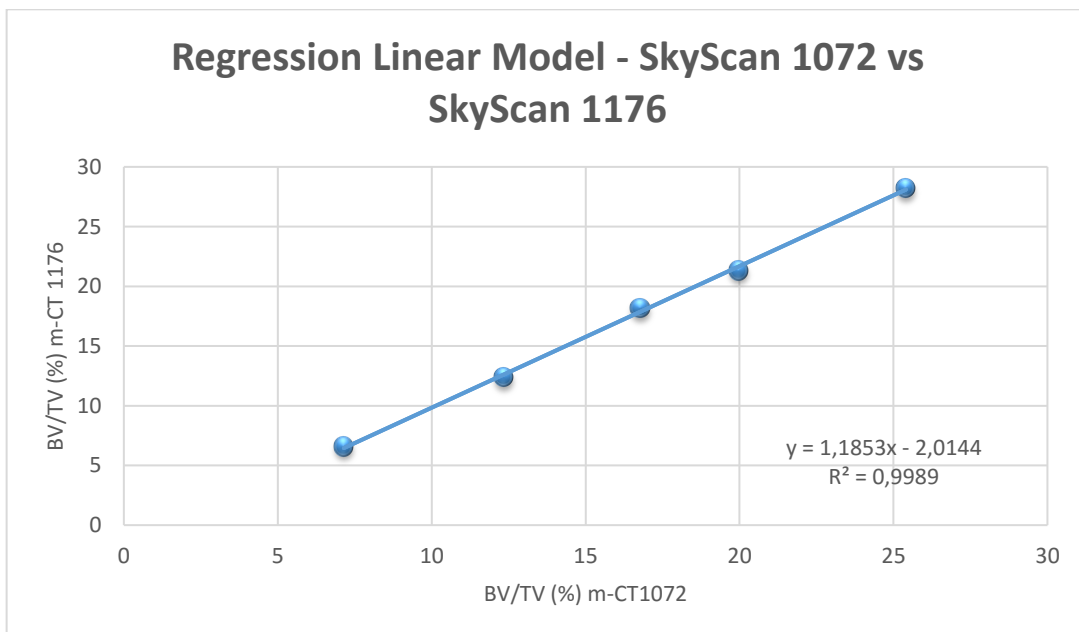

Fig.37 – Regression Linear Model for BV/TV (%) values obtained with SkyScan 1072 (threshold 117) and those obtained with SkyScan 1176 (threshold 123).

R^2 gives some information about the fit of each model. In this case, the coefficient of determination R^2 is a statistical measure of how well the

regression line approximates the real data points. The results of $R^{2=}$ 0,9989 indicates that the regression line almost perfectly fits the data. For this reason, all the calculations in the segmentation of images obtained with the SkyScan 1176 scanners will be carried out using 123 as threshold value.

5.2 Analysis of measurements performed on SAMPLE type 1

Sample type 1 is characterized by 5 cylindrical biopsies from femoral bone of cadavers with only trabecular tissue embedded in PMMA. The scans were performed with SkyScan 1176 and both Cone Beam Newton 5G devices (installed in Brescia and Verona). For this reason, the parameter BV/TV (%), Tb.Th (mm) and Tb.Sp (mm), which are good descriptors of the trabecular structure, were calculated.

The method of the Minimum Variation was used again to calculate the optimal threshold value to process the images scanned with the NewTom 5G Cone Beam CT. The obtained results have quantified **157** as threshold value for the device installed at "Spedali Civili" of Brescia, while a value of **100** for the scanner installed at Verona QR. Since for Sample type 1 scans performed with micro-CT SkyScan 1072 were available, the calculation of each parameter was also performed on these data for the comparison with the two Cone Beam CT devices.

In the following graphs the values of the bone parameters calculated from the cone beam CT images are reported on the *y*-axis, while the corresponding values, obtained from micro-CT, are on *x*-axis. For each graph the equation of the linear regression and the corresponding coefficient of determination are reported.

SAMPLE type 1	BV/TV (%) SkyScan 1072	BV/TV (%) SkyScan 1176	BV/TV (%) NewTom 5G (Brescia)	BV/TV (%) NewTom 5G (Verona)
Specimen 1	12,4 ± 0,3	12,4 ± 0,9	7,2 ± 0,4	7,4 ± 0,4
Specimen2	20,1 ± 0,5	21,3 ± 1,6	32,9 ± 1,6	33,3 ± 1,6
Specimen 3	7,14 ± 0,17	6,5 ± 0,5	4,4 ± 0,2	1,21 ± 0,06
Specimen4	16,8 ± 0,4	18,1 ± 1,3	14,6 ± 0,7	19,3 ± 0,9
Specimen 5	25,4 ± 0,6	28 ± 2	28,9 ± 1,4	46 ± 2

Tab- 3 BV/TV (%) values calculated on the images obtained with different scanners using the previously defined thresholds for segmentation.
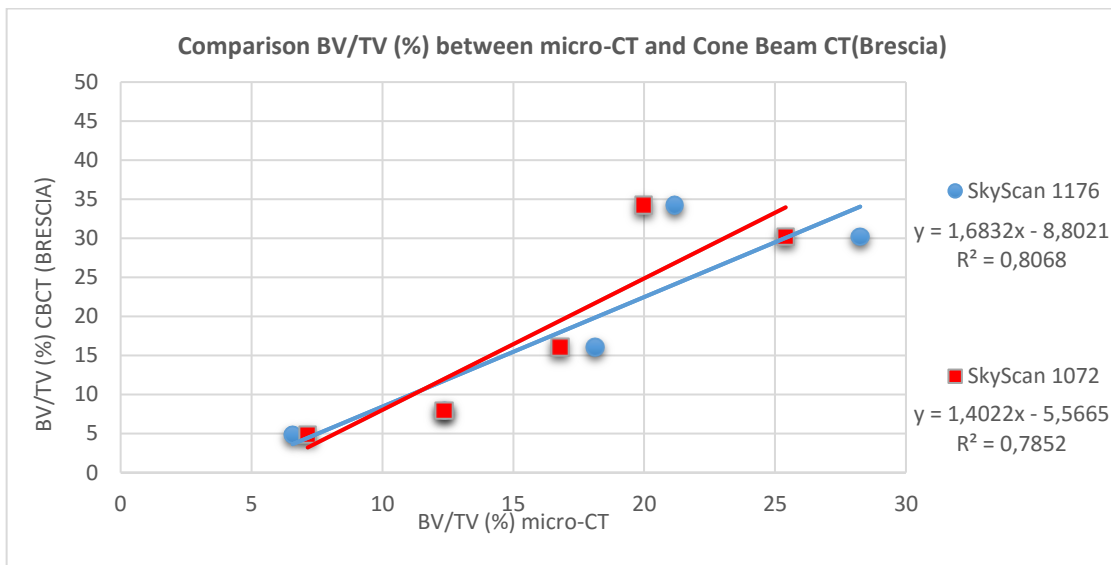
Fig 38 – BV/TV values obtained by means of micro-CT (SkyScan 1072 and SkyScan 1176) and Cone Beam CT NewTom 5G in Brescia.
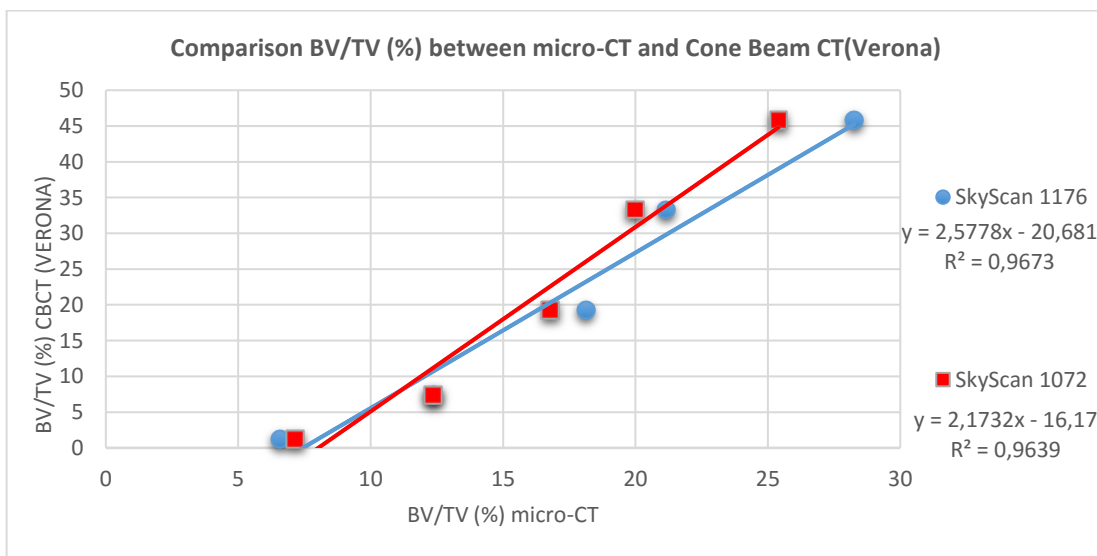

Fig 39 - BV/TV values obtained by means of micro-CT (SkyScan 1072 and SkyScan 1176) and Cone Beam CT NewTom 5G in Verona.

SAMPLE type 1	Tb.Th (mm) SkyScan 1072	Tb.Th (mm) SkyScan 1176	Tb.Th (mm) NewTom 5G (Brescia)	Tb.Th (mm) NewTom 5G (Verona)
Specimen 1	0,1559 ± 0,0012	0,166 ± 0,004	0,365 ± 0,018	0,331 ± 0,016
Specimen2	0,1916 ± 0,0015	0,208 ± 0,005	0,49 ± 0,02	0,44 ± 0,02
Specimen 3	0,1391 ± 0,0011	0,145 ± 0,004	0,375 ± 0,018	0,307 ± 0,015
Specimen4	0,1492 ± 0,0012	0,163 ± 0,004	0,42 ± 0,02	0,384 ± 0,019
Specimen 5	0,2195 ± 0,0017	0,251 ± 0,006	0,58 ± 0,03	0,62 ± 0,03

Tab 4 – Tb.Th (mm) values calculated on the images obtained with different scanners using the previously defined thresholds for segmentation.
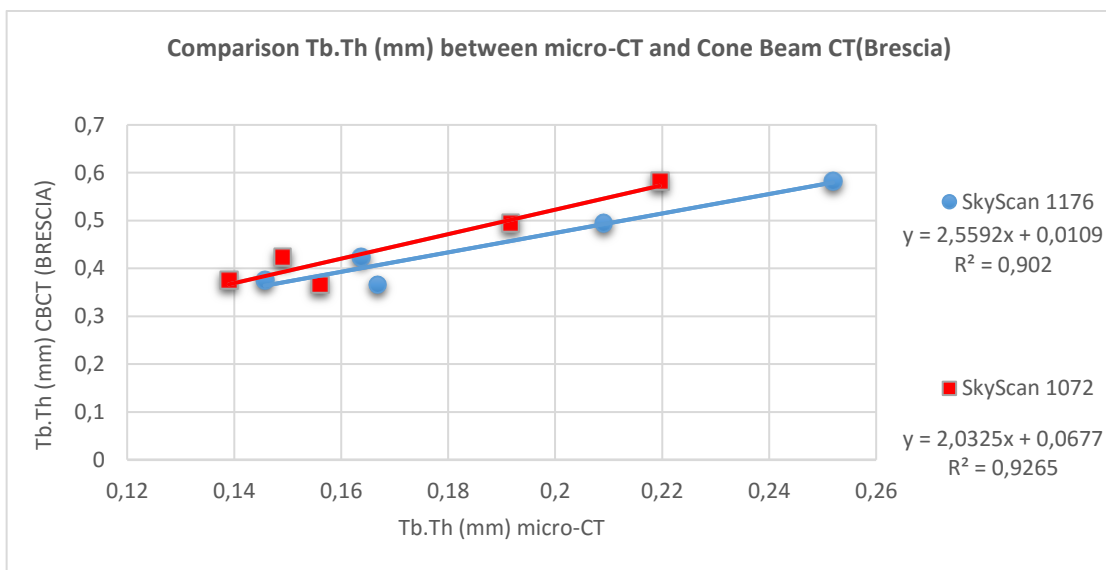

Fig 40 – Tb.Th (mm) values obtained by means of micro-CT (SkyScan 1072 and SkyScan 1176) and Cone Beam CT NewTom 5G in Brescia.
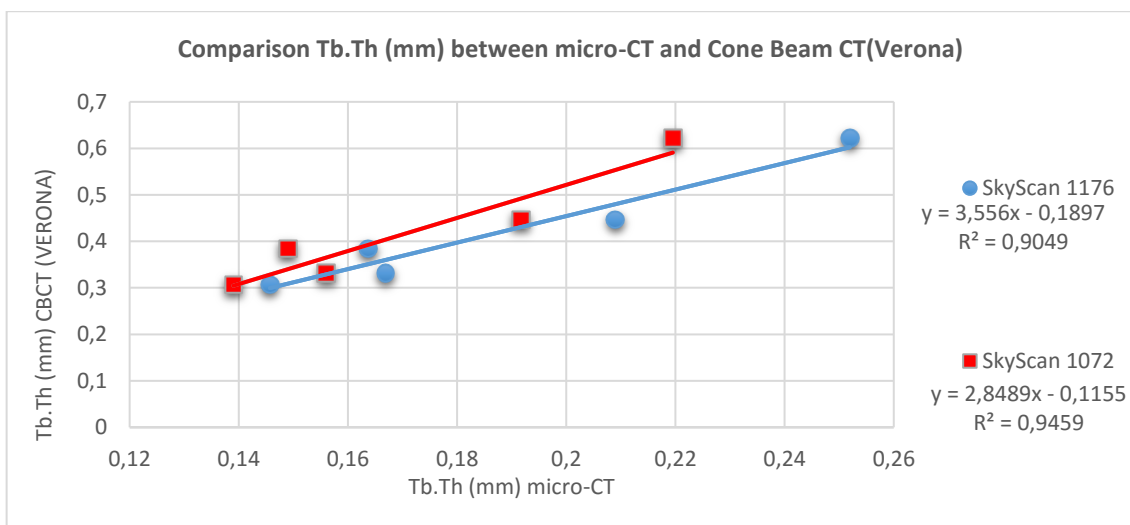

Fig 41 – Tb.Th (mm) values obtained by means of micro-CT (SkyScan 1072 and SkyScan 1176) and Cone Beam CT NewTom 5G in Verona.

SAMPLE type 1	Tb.Sp (mm) SkyScan 1072	Tb.Sp (mm) SkyScan 1176	Tb.Sp (mm) NewTom 5G (Brescia)	Tb.Sp (mm) NewTom 5G (Verona)
Specimen 1	0,921 ± 0,014	0,94 ± 0,02	1,62 ± 0,08	1,59 ± 0,08
Specimen2	0,76 ± 0,012	0,77 ± 0,02	0,95 ± 0,04	0,86 ± 0,04
Specimen 3	1,074 ± 0,017	1,12 ± 0,03	2,20 ± 0,11	3,01 ± 0,15
Specimen4	0,647 ± 0,011	0,66 ± 0,01	1,49 ± 0,07	1,19 ± 0,06
Specimen 5	0,643 ± 0,011	0,63 ± 0,01	1,07 ± 0,05	0,80 ± 0,04

Tab 5 – Tb.Sp (mm) values calculated on the images obtained with different scanners using the previously defined thresholds for segmentation.
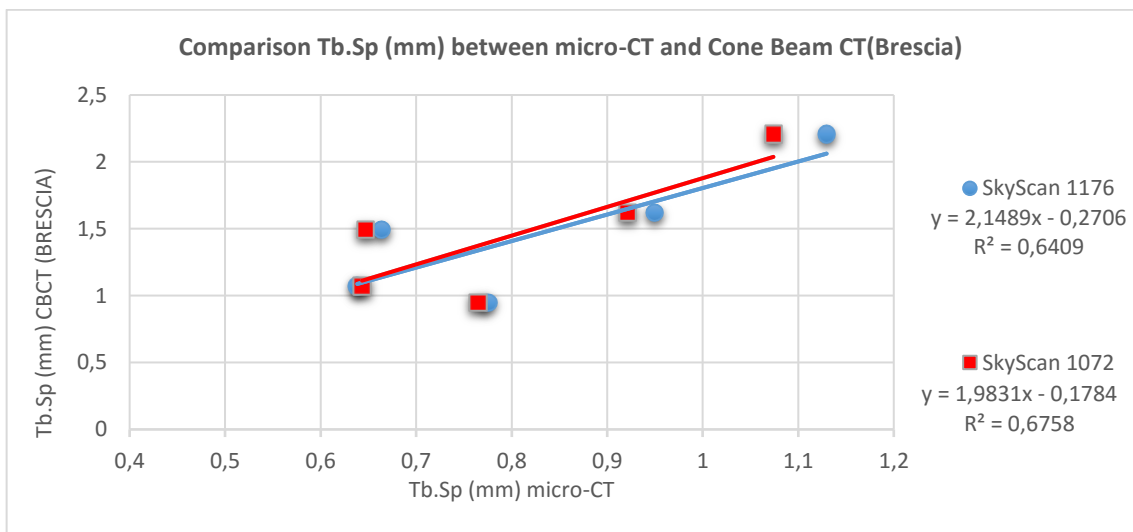

Fig 42 – Tb.Sp (mm) values obtained by means of micro-CT (SkyScan 1072 and SkyScan 1176) and Cone Beam CT NewTom 5G in Brescia.
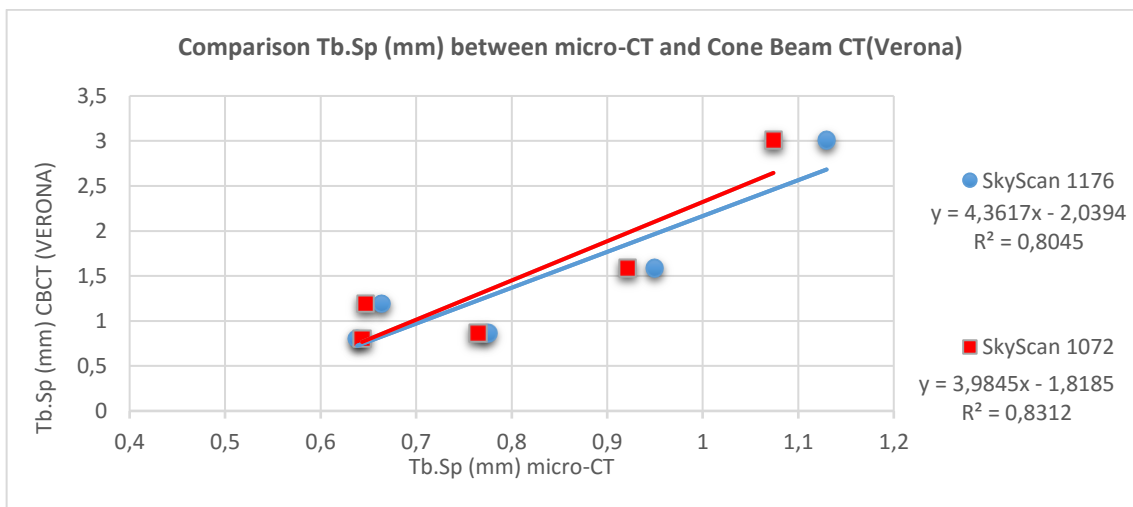

Fig 43 – Tb.Sp (mm) values obtained by means of micro-CT (SkyScan 1072 and SkyScan 1176) and Cone Beam CT NewTom 5G in Verona.

As the graphs show, the obtained results are more than satisfactory. In most cases (except in the evaluation of Tb.Sp compared with NewTom 5G of Brescia, $p<0.05$), the coefficients of determination R^2 range from 0,8 to 0,96 ($p<0.008$). Therefore, not only a positive correlation of data is present but also a very strong association of variables.

However, it is worth noting that the two Cone Beam CT presented a different behavior. Although both devices are the same model, it has to be mentioned that the NewTom 5G installed at "Spedali Civili"-Brescia has a very intense clinical load, while the NewTom 5G installed at QR-Verona is mostly dedicated to research and development and reasonably it does not have the same amount of use. In any case, it can be said that the outcome of the test satisfies the initial premises.

5.3 Analysis of measurements performed on SAMPLE type 2

For Sample type 2, which includes 3 biopsies of tibial bone from cadavers characterized by only cortical tissue, a technique based on the distribution of the gray levels present on images was used to determinate the threshold value. It is a purely subjective operation since it is based on the "good eye" operator and his experience. To segment the images scanned with micro-CT SkyScan 1176, a threshold value of **148** (for cortical bone) was chosen, while the correspondent threshold value for CBCT NewTom 5G (Brescia) was found at **175**. The Tables below show the values of the Degree of Anisotropy and Total Porosity estimated by Ct-Analyser software (Bruker) with the thresholds mentioned above, while in the graphs the corresponding Linear Regression Model is reported.

SAMPLE type 2	DA SkyScan 1176	DA NewTom 5G (Brescia)
Specimen 1	1,94 ± 0,15	2,81 ± 0,14
Specimen2	2,05 ± 0,16	3,10 ± 0,15
Specimen 3	2,24 ± 0,18	4,4 ± 0,2

Tab 6 – Degree of Anisotropy values calculated from images obtained with micro-CT SkyScan 1176 and Cone Beam CT NewTom 5G in Brescia.
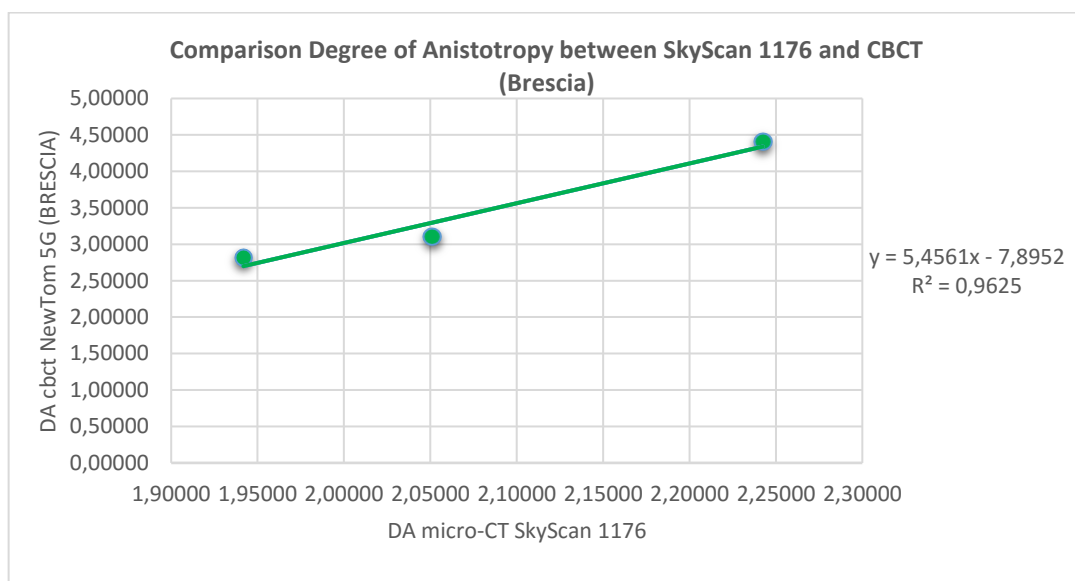

Fig. 44 – Comparison of the Degree of Anisotropy values calculated on images obtained with Micro-CT SkyScan 1176 and Cone Beam CT NewTom 5G in Brescia.

SAMPLE type 2	Po(tot)(%) SkyScan 1176	Po(tot)(%) NewTom 5G (Brescia)
Specimen 1	2,24 ± 0,07	0,66 ± 0,03
Specimen2	1,96 ± 0,06	0,71 ± 0,03
Specimen 3	1,49 ± 0,05	0,40 ± 0,02

Tab 7 – Total Porosity values (%) calculated from images obtained with micro-CT SkyScan 1176 and Cone Beam CT NewTom 5G in Brescia.
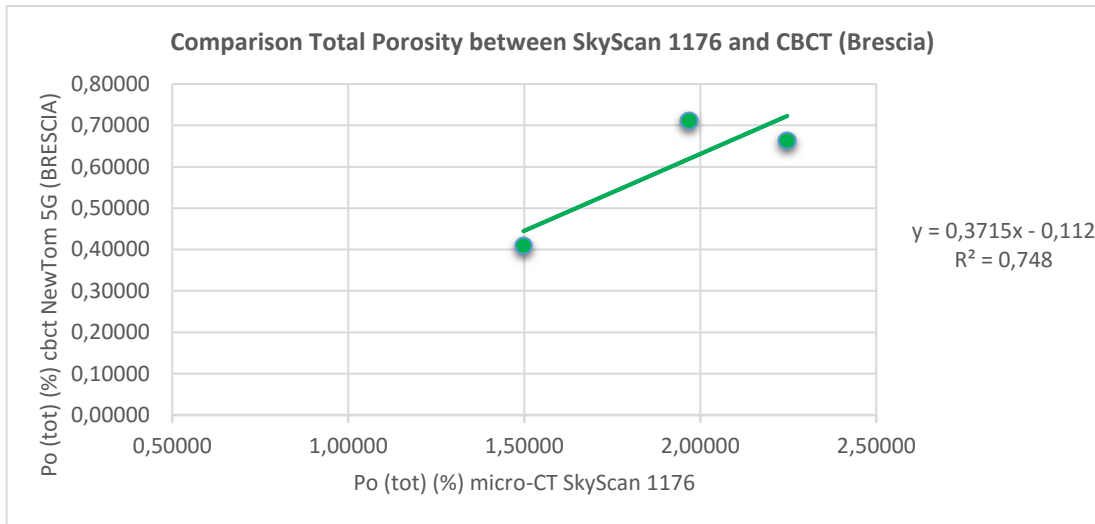
Fig. 45 – Comparison of the Total Porosity (%) values calculated on images obtained with Micro-CT SkyScan 1176 and Cone Beam CT NewTom 5G in Brescia.

Also for the samples of group 2, through the Linear Regression graph, a good correlation between the data is found, with coefficient of determination R^2 equal to respectively 0,96 (p<0.1) and 0,74 (p<0.3).

5.4 Analysis of measurements performed on SAMPLE type 3

The comparison for Sample type 3 was done on images scanned with micro-Ct SkyScan 1176 and Cone Beam CT NewTom 5G installed at QR in Verona. Seventeen thoracic and lumbar vertebrae of cadavers with both trabecular and cortical bone were analyzed. Vertebrae belonged to severely osteoporotic donor subjects. With a polygonal ROI interpolated throughout the dataset, the BV/TV (%) was calculated by means of Ct-Analyser software (Bruker). Subsequently a comparison of the two methods of imaging discussed until now was performed.

The optimal threshold adopted for the image segmentation is **97** and it is equal to the arithmetic mean of the thresholds calculated for each sample with the method of Minimum Variation. In this case the

variability of the thresholds was very high (from 48 to 133), but the aim was to find a global threshold valid for all the samples.

SAMPLE type 3	BV/TV (%) SkyScan 1176	BV/TV (%) NewTom 5G (Verona)
Specimen 1	13,51 ± 1,02	59±3
Specimen2	12,8 ± 0,9	17,5 ± 0,8
Specimen 3	3,2 ± 0,2	0,018 ± 0,001
Specimen 4	3,0 ± 0,2	0*
Specimen 5	3,6 ± 0,2	0,012 ± 0,001
Specimen 6	4,3 ± 0,3	27,3 ± 1,3
Specimen 7	25,1 ± 1,6	3,43 ± 0,17
Specimen 8	12,5 ± 0,9	17,1 ± 0,8
Specimen 9	8,1 ± 0,6	0,94 ± 0,04
Specimen 10	3,6 ± 0,2	0,014 ± 0,001
Specimen 11	5,9 ± 0,5	0,018 ± 0,001
Specimen 12	5,7 ± 0,4	22,59 ± 1,13
Specimen 13	5,6 ± 0,4	38,0 ± 1,9
Specimen 14	7,6 ± 0,6	2,87 ± 0,14
Specimen 15	6,8 ± 0,5	1,41 ± 0,07
Specimen 16	7,9 ± 0,6	19,2 ± 0,9
Specimen 17	8,2 ± 0,6	0,45 ± 0,02

Tab 8 – BV/TV (%) values calculated from the images obtained with SkyScan 1176 and NewTom 5G in Verona.

* it is not a real value; Software is unable to calculate it.

From the table 8 it can be seen a certain discrepancy between the obtained values. The same discrepancy is even more clear in Fig. 46, in which the coefficient of determination $R^2 = 0,03$ shows a total lack of correlation between the data.
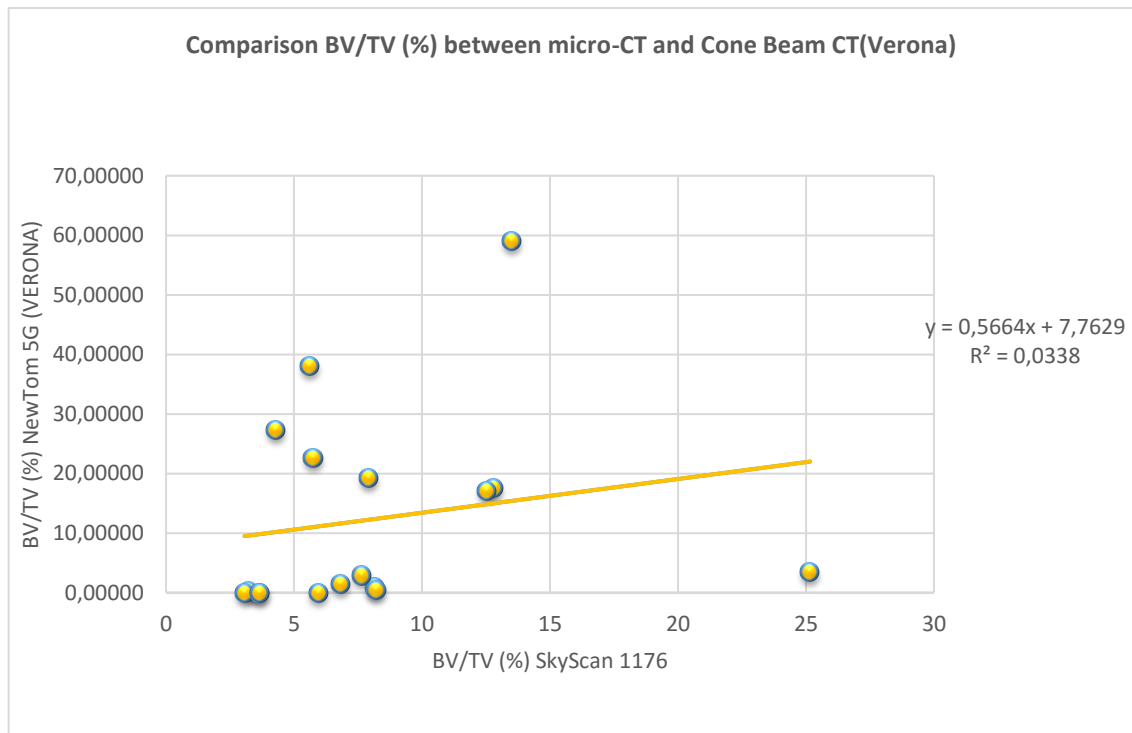
Fig. 46– Comparison of BV/TV (%) values calculated on the images obtained with micro-CT SkyScan 1176 and Cone Beam CT NewTom 5G in Verona.

To improve the obtained results, a Sharpening filter (implemented in Ct-Analyser Software) was applied to images scanned with Cone Beam CT. The obtained values slightly improve but the low coefficient of determination obtained from Linear Regression Model (Fig. 47) confirms the total non-correlation between the data.

SAMPLE type 3	BV/TV (%) SkyScan 1176	BV/TV (%) NewTom 5G (Brescia) **SHARPENING FILTER**
Specimen 1	13,51 ± 1,02	55,1 ± 2,7
Specimen2	12,8 ± 0,9	28,2 ± 1,4
Specimen 3	3,2 ± 0,2	2,38 ± 0,12
Specimen 4	3,0 ± 0,2	0,067 ± 0,003
Specimen 5	3,6 ± 0,2	0,014 ± 0,007
Specimen 6	4,3 ± 0,3	32,29252
Specimen 7	25,1 ± 1,6	10,9 ± 1,6
Specimen 8	12,5 ± 0,9	22,65 ± 1,13
Specimen 9	8,1 ± 0,6	4,2 ± 0,2
Specimen 10	3,6 ± 0,2	0,167 ± 0,008
Specimen 11	5,9 ± 0,5	0,094 ± 0,004
Specimen 12	5,7 ± 0,4	18,5 ± 0,9
Specimen 13	5,6 ± 0,4	33,6 ± 1,6
Specimen 14	7,6 ± 0,6	8,2 ± 0,4
Specimen 15	6,8 ± 0,5	5,4 ± 0,2
Specimen 16	7,9 ± 0,6	22,75 ± 1,13
Specimen 17	8,2 ± 0,6	1,75 ± 0,08

Tab 8 – BV/TV (%) values calculated from the images obtained with SkyScan 1176 and NewTom 5G in Verona, after the application of a Sharpening Filter
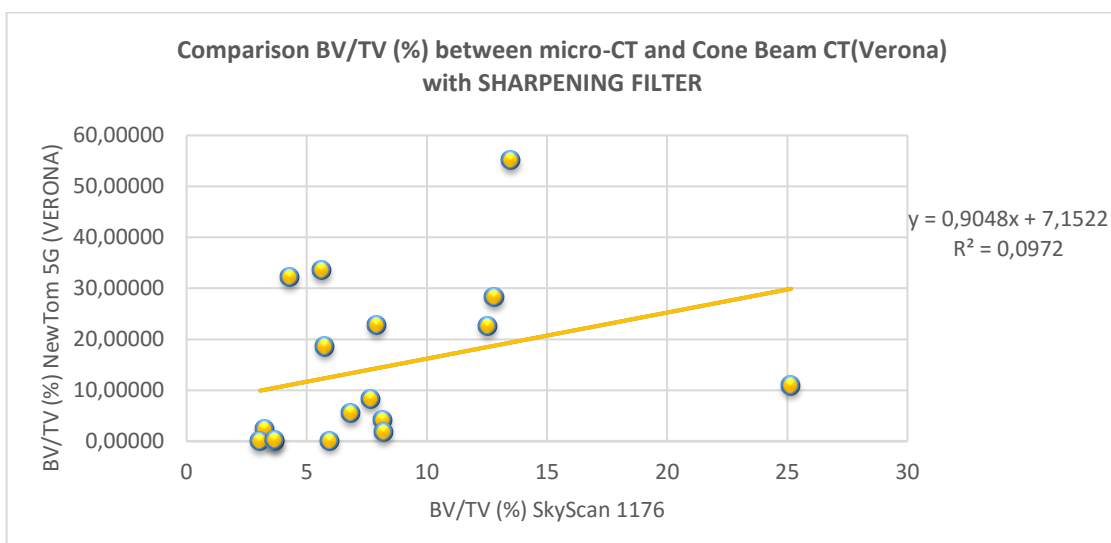

Fig. 47 – Comparison of BV/TV (%) values calculated on the images obtained with micro-CT SkyScan 1176 and Cone Beam CT NewTom 5G in Verona, after the application of a Sharpening Filter.

CHAPTER 6
Discussion of Results

6.1 Considerations about the measurements performed on the 3 types of Sample

In the Chapter 5, the results, obtained after the laborious measurements on the three available types of samples, have been shown.

The purpose of this thesis is to compare the morpho-structural parameters that characterize the bone tissue and in particular the trabecular tissue, calculated on images obtained through two methods of tomographic imaging.

For the first two types of samples (5 biopsies of femoral bone and 3 biopsies of tibial bone), as documented also with the graphs in paragraphs **5.2** and **5.3**, the obtained results show a significant correlation between the two sets of data *using a global threshold value* for the segmentation of the images. This demonstrate, therefore, a positive outcome for the comparison of the two methods of tomographic imaging used for all the tests and it gives a positive answer to the main question of this thesis. It is, however, worth pointing out that the Samples type 1 and 2 correspond to extremely ideal cases: bone tissue, completely trabecular or completely cortical, of small dimensions, embedded in PMMA that has a coefficient of attenuation similar to that of water.

As regards the Sample type 3, instead, the same positive answer was not found. Indeed, the negative results certainly exclude the use of a global threshold for image processing. However, it is good to pay close

attention to the conditions in which the samples were scanned: we are in a real case that is not remotely close to the optimal conditions of the other (small specimens embedded in biocompatible material).

Several could be the causes that can be attributed to these results: for example, the scan mode (which was done in air), the quality of the beam, the use of a little appropriate software for the processing of the images (Ct- Analyser was created above all for the processing of micro-CT images), and, not least, the pathological severity of the disease from which the donors were suffering. In fact it is easy to see that many samples analyzed had a really to low BV/TV (about 3 %).

A possible explanation for the poor results obtained for the Sample type 3 can also be attributed to the use, for the calculation of structural parameters, of a software that necessarily requires the binarization of the images' dataset in only white or black pixels. In this case, it becomes very difficult, even to the naked eye, to distinguish what is bone, what is marrow or water when lower spatial resolutions than those obtained by micro-tomography (defined as "gold standard") are involved.

In fact, micro-CT is a powerful and consolidated tool for the three-dimensional investigation of bone samples, allowing a quantitative characterization of the microarchitecture at high resolution and in a non-destructive way.

The use of bone tissue descriptors, already present in literature, which avoid the segmentation of the images, could be very efficient in evaluating the comparison between micro-CT and Cone Beam CT.

6.2 Future Developments

The research will proceed with the analysis of descriptors of the bone quality based on structural tensors, such as the fabric tensor or the gradient structure tensor.

A preliminary attempt has already been made through the use of the Gradient Structure Tensor (GST). Structure tensors are a matrix representation of partial derivative information. In the field of image processing and computer vision, it is typically used to represent the gradient or "edge" information. The term "tensor" refers to a representation of an array of data where L1, L2, L3 and e1, e2, e3 are the eigenvalues and eigenvectors respectively. These components can be visualized as 3D ellipses where the radii are equal to the eigenvalues in descending order and directed along their corresponding eigenvectors. Using gradient-based structure tensors, local patterns of contours and surfaces may be inferred through a diffusion process (Nicolescu & Medioni, 2003). Many studies demonstrated, for example, that the method to determine trabecular main direction in situ is GST. (Wolfram, Schmitz, Heuer, Reinehr, & Wilke, 2009). Knowing the main direction, a transverse isotropic fabric tensor can be constructed.

In the attempt abovementioned, a Matlab implementation available online was used (Arseneau, 2006); it has produced partial results, applicable, however, only in the 2D case. An *ad hoc* implementation could give more satisfactory results applicable in 3D, in order to confirm the positive answer found in Sample type 1 and 2 also in real cases that undoubtedly have poor conditions, much more difficult to manage.

REFERENCES

Adams, J. E. (2009). Quantitative computed tomography. *European Journal of Radiology*, *71*(3), 415–424. http://doi.org/10.1016/j.ejrad.2009.04.074

Anderson, H. C. (2003). Matrix vesicles and calcification. *Current Rheumatology Reports*, *5*(3), 222–226. http://doi.org/10.1007/s11926-003-0071-z

Arseneau, S. (2006). http://www.mathworks.com.

Bone Density Scan. (n.d.). Retrieved from http://www.rwrad.com/Bone-Density.html

Buckwalter, J. A., Glimcher, M. J., Cooper, R. R., & Recker, R. (1996). Bone biology. I: Structure, blood supply, cells, matrix, and mineralization. *Instructional Course Lectures*, *45*, 371–86. http://doi.org/10.3390/jfb1010022

Celenk, C., & Celenk, P. (2008). Bone Density Measurement Using Computed Tomography. In *Computed Tomograpy - Clinical Applications* (pp. 123–136).

Clifford J. Rosen, Roger Bouillon, Juliet E. Compston, V. R. (2013). *Primer on the Metabolic Bone Diseases and Disorders of Mineral Metabolism*. (Wiley-Blackwell, Ed.).

Compston, J. (2006). Bone quality: what is it and how is it measured? *Arquivos Brasileiros de Endocrinologia E Metabologia*, *50*(4), 579–585. http://doi.org/S0004-27302006000400003 [pii]

Cosman, F., de Beur, S. J., LeBoff, M. S., Lewiecki, E. M., Tanner, B., Randall, S., & Lindsay, R. (2014). Clinician's Guide to Prevention and Treatment of Osteoporosis. *Osteoporosis International*, *25*(10), 2359–2381. http://doi.org/10.1007/s00198-014-2794-2

Cowin, S., & Telega, J. (2003). Bone Mechanics Handbook, 2nd Edition. -. In *Applied Mechanics Reviews* (Vol. 56, p. B61). http://doi.org/10.1115/1.1579463

Dendy, P. P., Heaton, B., & Cameron, J. (2001). Physics for Diagnostic Radiology. *Medical Physics*. http://doi.org/10.1118/1.1350686

Ding, M., Odgaard, A., & Hvid, I. (1999). Accuracy of cancellous bone volume fraction measured by micro-CT scanning. *Journal of Biomechanics*, *32*(3), 323–326. http://doi.org/10.1016/S0021-9290(98)00176-6

Elliott, J. C., & Dover, S. D. (1982). X-ray Microtomography. *Journal of Microscopy*, *126*(2), 211–213. http://doi.org/10.1111/j.1365-2818.1982.tb00376.x

Florencio-Silva, R., Rodrigues, G., Sasso, S., Sasso-Cerri, E., Simões, M. J., & Cerri,

P. S. (2015). Biology of Bone Tissue: Structure, Function, and Factors That Influence Bone Cells. *BioMed Research International*, 1–17. http://doi.org/10.1155/2015/421746

Franz-Odendaal, T. A., Hall, B. K., & Witten, P. E. (2006). Buried alive: How osteoblasts become osteocytes. *Developmental Dynamics*. http://doi.org/10.1002/dvdy.20603

Gilbert SF. Developmental Biology. (2000). Osteogenesis: The Development of Bones. *Development Biology: 6th Edition*, http://www.ncbi.nlm.nih.gov/books/NBK10056/. http://doi.org/10: 0-87893-243-7

Goldman, L. W. (2007). Principles of CT and CT technology. *Journal of Nuclear Medicine Technology*, *35*(3), 115–28; quiz 129–30. http://doi.org/10.2967/jnmt.107.042978

Goulet, R. W., Goldstein, S. A., Ciarelli, M. J., Kuhn, J. L., Brown, M. B., & Feldkamp, L. A. (1994). The relationship between the structural and orthogonal compressive properties of trabecular bone. *Journal of Biomechanics*, *27*(4). http://doi.org/10.1016/0021-9290(94)90014-0

Guglielmi, G. (2010). Assessment of Bone Quality and Structure. *Clin Cases Miner Bone Metab.*

Guglielmi, G., Grimston, S. K., Fischer, K. C., & Pacifici, R. (1994). Osteoporosis: diagnosis with lateral and posteroanterior dual x-ray absorptiometry compared with quantitative CT. *Radiology*, *192*(3), 845–850. http://doi.org/10.1148/radiology.192.3.8058958

Hildebrand, T., & Rüegsegger, P. (1997). A new method for the model-independent assessment of thickness in three-dimensional images. *Journal of Microscopy*, *185*(1), 67–75. http://doi.org/10.1046/j.1365-2818.1997.1340694.x

Horton W A. (1990). The biology of bone growth. *Growth Genet. Horm*, (6(2):1–3).

Hubbell, J. H., & Seltzer, S. M. (1995). *Tables of X-Ray mass attenuation coefficients and mass energy-absorption coefficients 1 keV to 20 MeV for Elements Z=1 to 92 and 48 Additional substances of Dosimetric Interest. http://physics.nist.gov/xaamdi*. Retrieved from http://www.nist.gov/pml/data/xraycoef/index.cfm

Issever, A. S., Link, T. M., Kentenich, M., Rogalla, P., Burghardt, A. J., Kazakia, G. J., … Diederichs, G. (2010). Assessment of trabecular bone structure using MDCT: Comparison of 64- and 320-slice CT using HR-pQCT as the reference standard. *European Radiology*, *20*(2), 458–468. http://doi.org/10.1007/s00330-009-1571-7

J Van Dessel, Y Huang, M Depypere, I Rubira-Bullen, F. M. and R. J. (2013). A

comparative evaluation of cone beam CT and micro-CT on trabecular bone structures in the human mandible. *Dentomaxillofac Radiology*.

Jerrold T. Bushberg, J. Anthony Seibert, Edwin M. Leidholdt Jr., J. M. B. (2002). *The Essential Physics of Medical Imaging (2nd Edition)*. (Lippincott Williams & Wilkins, Ed.).

Kak, A. C., Author, Slaney, M., Wang, G., & Reviewer. (2002). Principles of Computerized Tomographic Imaging. *Medical Physics*, *29*, 107–107. http://doi.org/10.1118/1.1455742

Keith Gibbs. (2006). *Advanced Physics*. (C. U. Press, Ed.).

Liu, Y., Saha, P. K., & Xu, Z. (2012). Quantitative characterization of trabecular bone micro-architecture using tensor scale and multi-detector CT imaging. *Medical Image Computing and Computer-Assisted Intervention : MICCAI ... International Conference on Medical Image Computing and Computer-Assisted Intervention*, *15*(Pt 1), 124–131.

Melton. (1992). No Title. Retrieved from http://www.orthop.washington.edu/?q=patient-care/articles/bone/osteoporosis.html

Naitoh, M., Aimiya, H., Hirukawa, A., & Ariji, E. (2010). Morphometric analysis of mandibular trabecular bone using cone beam computed tomography: an in vitro study. *The International Journal of Oral & Maxillofacial Implants*, *25*(6), 1093–8. Retrieved from http://www.ncbi.nlm.nih.gov/pubmed/21197484

Nicolescu, M., & Medioni, G. (2003). Motion segmentation with accurate boundaries - a tensor voting approach. *2003 IEEE Computer Society Conference on Computer Vision and Pattern Recognition, 2003. Proceedings.*, *1*(June). http://doi.org/10.1109/CVPR.2003.1211379

Noble, B. S. (2008). The osteocyte lineage. *Archives of Biochemistry and Biophysics*. http://doi.org/10.1016/j.abb.2008.04.009

Odgaard, A. (1997). Three-dimensional methods for quantification of cancellous bone architecture. *Bone*. http://doi.org/10.1016/S8756-3282(97)00007-0

Parfitt AM, Drezner MK, Glorieux FH, Kanis JA, Malluche H, Meunier PJ, Ott SM, R. R. (1987). Bone Histomorphometry: standardization of nomenclature, symbols and units. *Journal of Bone and Mineral Research 2*.

Parsa, A., Ibrahim, N., Hassan, B., van der Stelt, P., & Wismeijer, D. (2015). Bone quality evaluation at dental implant site using multislice CT, micro-CT, and cone beam CT. *Clinical Oral Implants Research*, *26*(1), e1–e7. http://doi.org/10.1111/clr.12315

Perilli. (2006). *Microtomographic techniques for the characterization of bone tissue*.

Poludniowski, G., Landry, G., DeBlois, F., Evans, P. M., & Verhaegen, F. (2009). SpekCalc: a program to calculate photon spectra from tungsten anode x-ray tubes. *Physics in Medicine and Biology*, *54*(19), N433–N438. http://doi.org/10.1088/0031-9155/54/19/N01

Reinbold, W. D., Genant, H. K., Reiser, U. J., Harris, S. T., & Ettinger, B. (1986). Bone mineral content in early-postmenopausal and postmenopausal osteoporotic women: comparison of measurement methods. *Radiology*, *160*(2), 469–78. http://doi.org/10.1148/radiology.160.2.3726129

Scarfe, W. C., Farman, A. G., & Sukovic, P. (2006). Clinical applications of cone-beam computed tomography in dental practice. *Journal (Canadian Dental Association)*, *72*(1), 75–80.

Skyscan. (2005). Structural parameters measured by the Skyscan™ CT-analyser software. In Skyscan Ed.; (Ed.), .

Van Staa, T. P., Dennison, E. M., Leufkens, H. G. M., & Cooper, C. (2001). Epidemiology of fractures in England and Wales. *Bone*, *29*(6), 517–522. http://doi.org/10.1016/S8756-3282(01)00614-7

Wolfram, U., Schmitz, B., Heuer, F., Reinehr, M., & Wilke, H. J. (2009). Vertebral trabecular main direction can be determined from clinical CT datasets using the gradient structure tensor and not the inertia tensor-A case study. *Journal of Biomechanics*, *42*(10), 1390–1396. http://doi.org/10.1016/j.jbiomech.2009.04.006

www.bruker.com. (n.d.).

www.newtom.it. (n.d.). Retrieved from http://www.newtom.it/en-us/products/newtom-5g

Yoshiko, Y., Candeliere, G. A., Maeda, N., & Aubin, J. E. (2007). Osteoblast autonomous Pi regulation via Pit1 plays a role in bone mineralization. *Molecular and Cellular Biology*, *27*(12), 4465–74. http://doi.org/10.1128/MCB.00104-07

Ziegler, S. I. (2005). Positron emission tomography: Principles, technology, and recent developments. *Nuclear Physics A*. http://doi.org/10.1016/j.nuclphysa.2005.02.067

ACKNOWLEDGMENTS